Thermomechanical coupling investigation in Ti-6Al-4V orthogonal cutting: experimental and numerical confrontation

Mahmoud Harzallah, Thomas Pottier, Rémi Gilblas, Yann Landon, Michel Mousseigne, Johanna Senatore

Thermomechanical coupling investigation in Ti-6Al-4V orthogonal cutting: Experimental and numerical confrontation

M. Harzallah [a,b,c,*], T. Pottier [a], R. Gilblas [a], Y. Landon [b], M. Mousseigne [b], J. Senatore [b]

[a] Institut Clément Ader (ICA), Université de Toulouse, CNRS, Mines Albi, UPS, INSA, ISAE-SUPAERO, Campus Jarlard, Albi CT Cedex 09 81013, France
[b] Institut Clément Ader (ICA), Université de Toulouse, CNRS, Mines Albi, UPS, INSA, ISAE-SUPAERO, 3 rue Caroline Aigle, Toulouse 31400, France
[c] Laboratoire Génie de Production (LGP), Université de Toulouse, École Nationale d'Ingénieurs de Tarbes (ENIT), 47 avenue d'Azereix, Tarbes 65016, France

Keywords:
Digital image correlation
Infrared thermography
Orthogonal cutting
Damage
Thermomechanical couplings
Behavior

A B S T R A C T

The constant industrial need of detail data on the chip formation meets with the lack of a physical understanding of the thermo-mechanical couplings during hard metal cutting. In the present paper, numerical and experimental investigations at micro scale (about 0.5×0.5 mm^2 area), is performed in order to highlight the mechanisms responsible for the poor Ti-6Al-4V machinability. In a first step, strain, strain-rates, temperatures, dissipated powers along with displacements, velocity and crack propagation are obtained at each pixel by means of VISIR apparatus. Experimental observations have highlighted the dependency of the physical phenomena to both cutting speed and rake angle and provide valuable evidences on the different nature of the coupling phenomenon. Secondly, a 3D FE orthogonal cutting model is then developed to bring a multi-scale comprehension of Ti-6Al-4V chip genesis and to predict the kinematics and thermal quantities. The numerical and experimental confrontation revealed the robustness of the developed FE model as well as its limits. Hence, the element deletion method and the friction model are identified as the main weak spots of the proposed FE model. Finally, a particular attention is paid to the chip formation steps and their impact on the final part.

1. Introduction

Titanium alloys, although widely used in the aerospace and biomedical industries, are known for their poor machinability [1]. Such a disadvantage results from (i) a low thermal conductivity, (ii) a high capacity to maintain strength at high temperature and (iii) the inability to generate continuous chip [2,3].

Numerous experimental studies on machining of titanium alloys have been carried out in order to investigate the Ti-6Al-4V machinability and to enhance the tool life as well as the surface integrity. Alternatively, several research works have been devoted to machining assistance technics such as laser [4–6], cryogenic [7,8] and High pressure assistances [9–11]. On the other hand, many researchers addressed comprehensive and exhaustive studies on the physical phenomena involved in Ti-6Al-4V machining [12,13]. Accordingly, three main theories are developed in order to explain the Ti-6Al-4V chip formation [3,14,15]. The first one supposes that the chip formation is based on adiabatic shear band induced by the thermal and strain softening in the material [16,17]. The second theory is based on cracks propagation along the shear plane [3,18,19]. It starts at the tool tip then reaches the free surface of the material. Finally, the last theory is the combination of the two aforementioned theories in which the adiabatic shear band is the precursor of a material failure leading to crack propagation [20,21].

The understanding of the thermo-mechanical mechanisms involved in chip formation is a very topical issue. The localized and rapid nature of the machining has prevented from a straight forward experimental access to these couplings. Therefore, researchers widely investigated the use of numerical simulation in understanding the material removal phenomenon. Accordingly, many numerical simulations of the machining process have been performed in recent years.

In order to describe the flow behavior of the material in machining, several works adopted the Johnson Cook constitutive model [22]. It dissociates hardening, viscous and thermal aspects by three independents terms. For aluminum machining, Mabrouki et al. [23] employed this law to understand the physical phenomena accompanying chip formation at various cutting speed. Atlati et al. [24] adopted the Johnson Cook law as well in order to characterize the segmentation process in machining. Ayed et al. [6] developed an orthogonal cutting FE model aiming at optimizing the parameters of laser assisted titanium alloy machining. Because of its popularity, an important number of identification of this model has been carried out in the last decade [25–28]. For this reason, Ducobu et al. [28] gathered 20 sets of Johnson–Cook parameters from the literature for Ti6Al4V and conducted a qualitative and quantitative selection of the most representative set of parameters by comparing the outputs of a Coupled Eulerian-Lagrangian orthogonal cutting model with the experimental results. Specially for the machining simulation

* Corresponding author.
E-mail address: mahmoud.harzallah@enit.fr (M. Harzallah).

of AISI 316L steel, Umbrello et al. [29] explored the effects of five different sets of J-C material constants using an orthogonal cutting model and by assessing the predicted cutting forces, chip morphology, temperature distributions and residual stresses. The authors observed that all the considered process output and, in particular the residual stresses are very sensitive to the Johnson–Cook's material constants.

Inspired from the Johnson Cook model, Harzallah et al. [20] proposed a new behavior model coupled in temperature and strain rate in order to describe the complex phenomena induced by machining. Orthogonal cutting simulations using this latter model proved its capability to predict correctly the Ti-6Al-4V chip formation. Calamaz et al. [15] proposed a new material constitutive law to analyze the chip formation and shear localization when machining titanium alloys. Ducobu et al. [3] conducted a numerical comparison between the Johnson Cook model and the new behavior developed by Calamaz (TanH model). They concluded that taking into account the thermal softening is not sufficient to represent the titanium alloy chip formation as the strain softening phenomena must also be considered. Nevertheless, the range of validity of these models remains dependent on the experimental calibration tests and parameters identification. Several pioneering numerical works has also been led at microscale in order to closely describe the influence of microstructure on the thermo-mechanical response [6,30]. The use of crystal plasticity models is the common way to implement the material heterogeneity at microscale both from an allotropic phase and lattice orientation stand point. Such work usually focuses on material that exhibit grain size in the same order of magnitude as the feed rate such as Ti17 in [6] for instance.

The damage criterion is the second significant modeling feature. Indeed, chip formation results from material decohesion [31]. Liu et al. [32] conducted an evaluation of six ductile fracture models and their applicability for metal cutting simulation. Among these damage models, they showed that the Wierzbicki fracture model [33] is the most comprehensive criterion to describe the chip removal. Conversely, its only drawback is the number of parameters to be calibrated (7 parameters), some of which are difficult to be obtained from experiments directly. Mabrouki et al. [23] proposed a coupling between material damage evolution and its fracture energy to describe the material separation in the orthogonal cutting simulation. This modeling strategy is adopted by several researchers and for different materials [6,24,34]. Owen and Vaz [31] used a fracture criterion with a failure softening model in order to describe void growth mechanism in titanium alloy machining.

Regarding the friction phenomenon, the lack of experimental data at the tool/chip interface has led Bäker et al. [35] to neglect it in their model. Nevertheless, in most studies, the Coulomb friction model is generally adopted [6,36]. Guo et al. [37] improved this approach since stick-slip phenomenon is observed at the tool/chip interface. Indeed, a Coulomb friction law and a Tresca stress limit model are used simultaneously. Zhang et al. [34] showed that the surface limiting shear stress is linked to the contact pressure and the coefficient of friction. Ben Abdelali et al. [38] and Bonnet et al. [39] developed a new friction model as a function of the sliding velocity. Both of these works are using dedicated tribometers for calibration sake. However, experimental calibration of such models remains weak due to the lack of in-situ information on the local sliding velocity.

Despite the constructive contributions of the aforementioned works to enhance the numerical model prediction, the validation and calibration of machining simulations on a global scale remains excessively limited, and is achieved by a few comparisons in terms of cutting forces and chip morphology [3,24]. The majority of these findings are based on Ex-situ and post-mortem investigations of the machining. It reports at least as many questions as answers because of lack of in-situ information regarding temperature, strain field, strain rate and stresses. In fact, the machining process remains eminently a thermomechanical problem which requires simultaneous measurements of the strain field and temperature in order to analyze and describe the couplings between them during the chip formation [19,40,41].

Thanks to thermal imaging and Digital Image Correlation (DIC) performances, strain field and temperature measurements in the machining process are now possible and offer complimentary information, at the microscopic level, to enrich, on the one hand the numerical simulation inputs (behavior, damage and friction models) and on the other hand the experimental and numerical confrontations [42,43].

Based on this approach, several devices have been setup allowing to access the region of cut and therefore to observe the chip formation mechanisms and extract the thermal and/or kinematics fields [44]. In order to assess the kinematic fields during AISI 1045-HR machining, Hijazi and Madhavan [40] developed a complex dedicated device composed of four non-intensified digital cameras set in dual frame mode to perform a 4 images acquisition at 1 MHz. Baizeau et al. [45] developed a new system for residual strains assessment during machining. This apparatus is composed by a high speed camera (switched in double frame mode) and a laser flash system dedicated for scene illumination which synchronized with the tool position. During machining of 100CrMo7 material, only double frames before, during, and after the cut were captured by the camera. Such technique allows to enhance the image quality at high cutting speed but it is not sufficient for a better description of the chip formation mechanisms.

For the thermal fields measurement during high-Speed Machining of 6061-T6 Aluminum Alloy, Kazban et al. [46] used an optical system based on focused array of mercury-cadmium-tellurium (HgCdTe) infrared detectors. This system includes a concave mirror with an aluminum coating and two flat mirrors with a gold coating to enhance the radiation reflectivity. Although it provides a good thermal measurement, a careful optical alignment of the system is required to ensure that the detectors are properly focused on the surface of the workpiece and properly positioned ahead of the tool tip.

In addition, several studies focused on both machining kinematics and thermal fields using some dedicated systems. For example, Zhang et al. [47] used a thermal and a high speed cameras which were placed on each workpiece side for the chip formation mechanisms analysis. This latter study adopted a plane strains and stresses hypothesis in order to associate material points for each workpiece face. Whitenton et al. [48] developed a new device for the understanding of the machinability difference between iron and steel at micro scale. It is based on a coupling between thermal and high speed cameras which focused on the same objective. This is a simultaneous synchronized visible and thermal imaging system which is composed of a thermal infrared camera and a visible camera. The main lens is a $\times 15$ reflective lens that passes both visible and infrared light. The cold mirror reflects the visible light to the visible camera and transmits infrared light to the thermal camera.

Inspired from the latter device, an optical apparatus called VISIR is developed and calibrated by Harzallah et al. [49] for a simultaneous in-situ chip formation observation and measurements. Accordingly, the present paper deals with an experimental and numerical investigation of kinematics and thermal fields in order to better understand the chip formation genesis. The experimental set-up, material of study and post-processing strategy are firstly presented. Then, experimental results are presented and discussed. In a second section, the FE model is detailed and a numerical/experimental confrontation is performed. The force, kinematics and thermal fields are used for comparison purpose. Finally a comprehensive discussion on the chip generation phenomenon is addressed.

2. Experimental approach

2.1. Acquisition and machining devices

Thanks to VISIR apparatus, the simultaneous measurement of strains, strain rates and temperatures at tool tip vicinity is possible. The development and calibrations of this apparatus are described in a previous communication [49]. As depicted in Fig. 1b the scene of cut is illuminated through a collimated white-light LED (~ 1 Watt) which is integrated

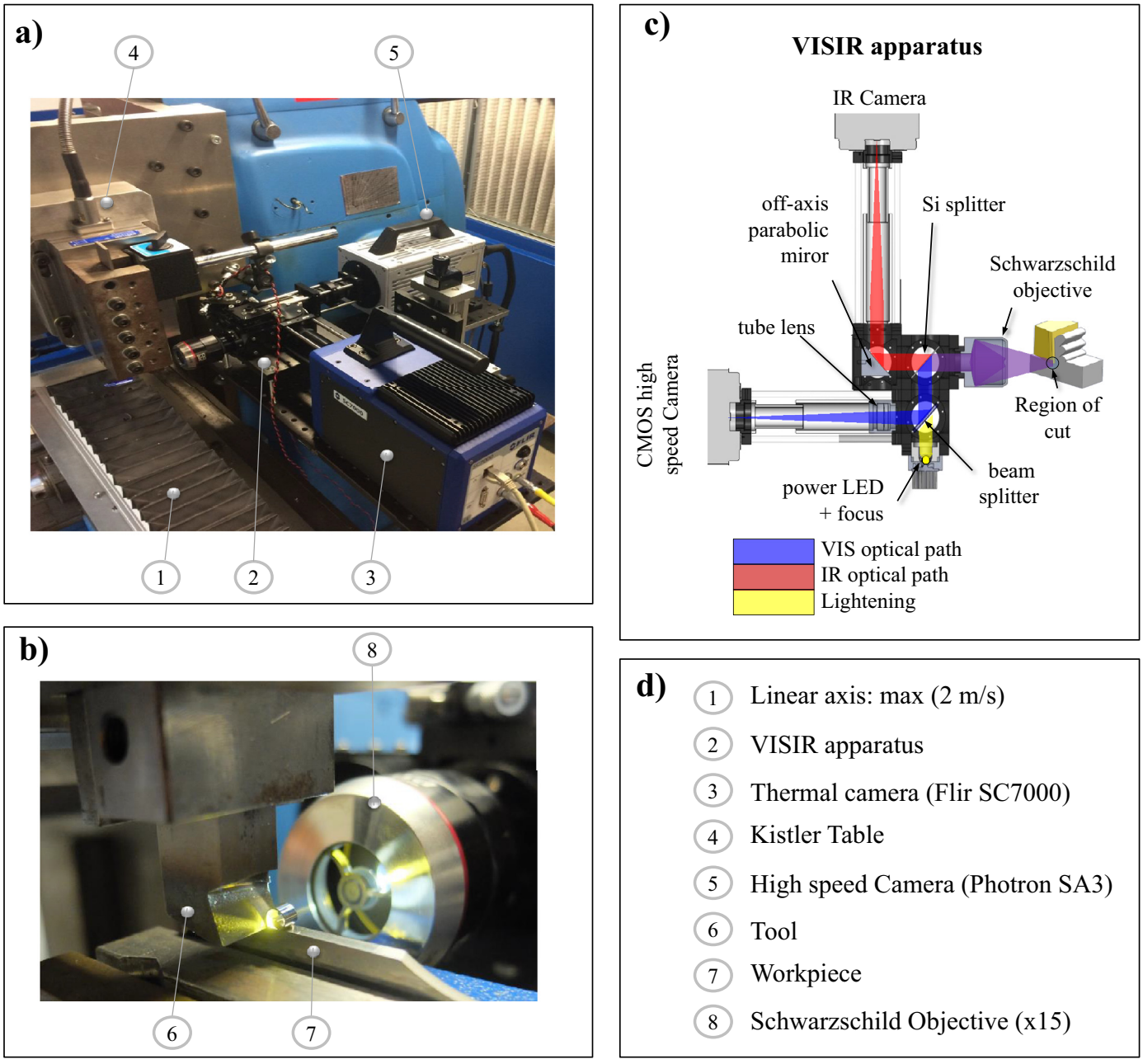

Fig. 1. Orthogonal cutting experimental setup: a) linear actuator, cutting tool and optical apparatus b) close up view of the cut c) VIS-IR apparatus detailed design d) nomenclature.

within the VISIR optical system. The radiation emitted by the workpiece and received by the reflective objective, over a range of wavelengths, is divided in two paths by the mean of a thin silicon splitter. This latter has the particularity to reflects all of radiation below 2 µm of wavelengths to the visible optical path and transmit the rest in the infrared optical path as described in the Fig. 1c. Then, the radiations are focused in the cameras sensors by means of mirrors. It must be mentioned that the chromatic aberrations are corrected through achromatic lens which were inserted in both paths.

In order to respect the orthogonal cutting configuration, a dedicated device, called DEXTER, made of a fixed tool and a linear actuator is used. This latter is fixed on the working plate of a conventional milling machine while the tool is fixed on the spindle head as presented in Fig. 1a. Cutting forces were measured using a 6-components dynamometer (Kistler 9257A).

2.2. *Workpiece and tool*

In the present work, the material under investigation is the Ti-6Al-4V (grade 5) titanium alloy. Its chemical composition was analyzed by spark-optical emission spectrometry and is reported in the Table 1. It should be mentioned that the studied material is tempered at 1000 K and the β-transus is around 1233 K. Its average grain size is measured around 19.2 µm.

The microstructure has been investigated through SEM and is described in Fig. 2a and b. It is characterized by a duplex microsturcture composed by primary α grains (hexagonal close-packed structure) surrounded by transformed β grains (body centre cubic structure).

The machined specimen ($100 \times 40 \times 3$ mm^3) was polished and etched in order to reveal the microstructure providing a natural speckle for digital image correlation (DIC).

Table 1
Chemical composition of the studied Ti-6Al-4V titanium alloy.

Ti %	Al %	V %	Fe %	Nb ppm	Si ppm	Cr ppm	Cu ppm	Ni ppm	Pd ppm	Mo ppm	Co ppm	C ppm	B ppm
88,98	6,395	4,282	0,156	410	280	180	180	130	120	110	110	72	29

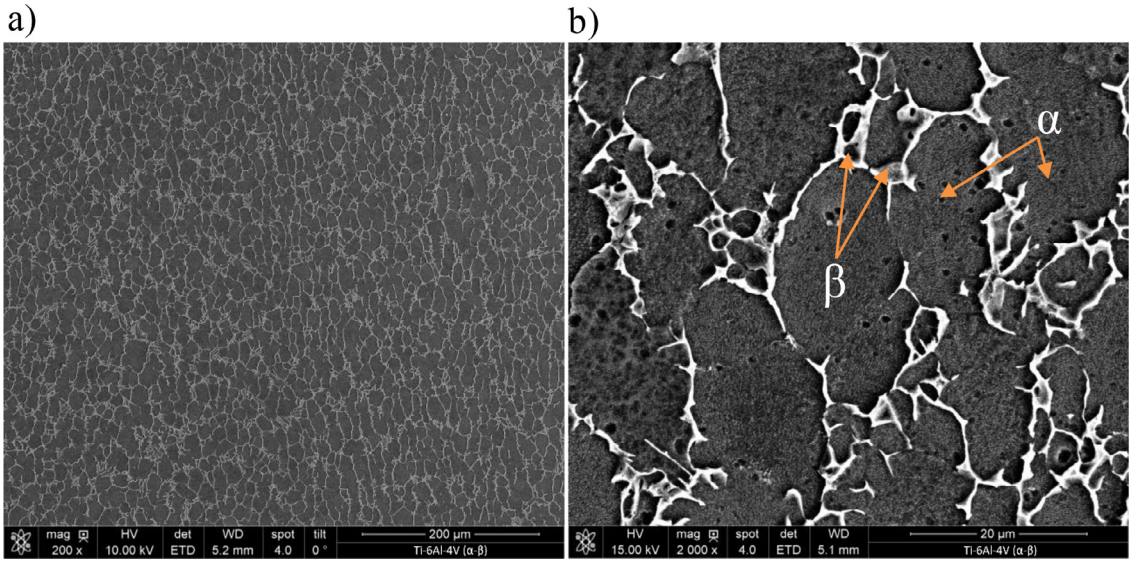

Fig. 2. (a) Initial microstructure of the machined Ti-6Al-4V (grade 5)- equiax structure (b) α and β phases of the material.

Table 2
Cutting velocity, feed and rake angles used.

	γ (°)	feed (mm)	Vc (m min^{-1})
Test 1	15	0.25	3
Test 2			15
Test 3	0		3
Test 4			15

Two uncoated carbide tools were used with two different rake angles ($\gamma = 0°, 15°$). They both present a clearance angle of $\alpha = 11°$ and a radius edge around 20 µm.

2.3. Acquisition and machining conditions

In order to overcome the motion blur phenomenon that occurs during image recording, a good compromise between the parameters for each camera (integration time, acquisition frequency, resolution, ...) and cutting conditions (cutting speed, feed, ...) must be achieved. Therefore, optical and machining parameters are fixed respectively for each test as described in Tables 2 and 3. For each tool, a feed of 0.25 mm is selected and two cutting speeds (Vc) are investigated.

The high speed camera on the visible optical path is a Photron Fastcam SA3. Its acquisition frequency F was set to 6000 fps and the exposure time (it_{vis}) varies between 30 and 50 µs depending on the cutting speed. A Flir SC7000 thermal camera was used in the infrared path (IR). It is set at 600 fps and an exposure time of $it_{IR} = 30$ µs providing a thermal image size of 160 × 128 pix^2. The simultaneous cameras triggering was conducted through a dedicated box synchronization.

For magnification assessment purpose, the metric ratio (R) was evaluated for the visible camera (Photron Fastcam SA3) at 1.133 µm/pix and at 1.981 µm/pix for the thermal camera. Readers could refer to [49] for the thermal camera calibration.

2.4. Experimental post-processing

2.4.1. Digital image correlation and kinematic fields calculations

The digital image correlation (DIC) is performed using 7D software [50]. As detailed in a previous work [49], the size of the subset is optimized through two approaches (Mean Intensity Gradient and Rigid body methods). Hence, it is set to 16 × 16 pix for a standard deviation of the measured displacements about 0.03 pix. However, cumulating such error over 50 images lead to a maximal error of 1.5 pix and therefore lead to errors on strain below 10% (if a 16 × 16 pix extensiometric basis is used).

The incremental correlation was used for kinematic fields calculations (i.e. displacements, strain and strain rate). This approach is recommended in the case of large deformation, high strain rate, out-of-plane motion and material decohesion [19,51]. In contrast, it requires a proper numerical processing in order to compute the cumulated displacements and strains. Accordingly, the cumulated displacement strategy detailed

Table 3
Optical parameters used for each test .

	it_{IR} (µs)	it_{vis} (µs)	R (µm/pix)		Image IR size (pix × pix)	Image visible size (pix × pix)	F (fps)	
			IR	visible			IR	visible
Test 1	50	50	1.981	1.133	160 × 128	512 × 512	600	6000
Test 2		30				384 × 352		
Test 3		50				512 × 512		
Test 4		30				512 × 512		

in [19,49] was used in order to enhance the assessment of the kinematic fields. Furthermore, the use of such a strategy offers a straight forward comparison between experimental results and numerical simulations in terms of logarithmic equivalent strain (HENKY) **H** and equivalent strain rate **D**. It's worth mentioning that the strain rate tensor is calculated by means of the displacement increments (ΔU_x, ΔU_y). The knowledge of this parameter offers a straight forward access to the velocity fields Vx and Vy. Assuming a constant capture rates of the images, it therefore comes $V_x = \Delta U_x/\Delta t$ and $V_y = \Delta U_y/\Delta t$. Then the components of the strain rate tensor D are:

$$\begin{cases} \mathbb{D}_{xx}(x_k, y_k, k) = \frac{\partial V_x(x_k,y_k,k)}{\partial x_k} \\ \mathbb{D}_{yy}(x_k, y_k, k) = \frac{\partial V_y(x_k,y_k,k)}{\partial y_k} \\ \mathbb{D}_{xy}(x_k, y_k, k) = \frac{1}{2}\left(\frac{\partial V_y(x_k,y_k,k)}{\partial x_k} + \frac{\partial V_x(x_k,y_k,k)}{\partial y_k}\right) \end{cases} \quad (1)$$

where (x_k, y_k) are the grid coordinates (identical for every image pair) for the image k. Readers can refer to [19] for more details.

2.4.2. Energy balance analysis

Coming from first and second laws of the thermodynamic, the heat equation is the basic ingredient to investigate the thermomechanical aspect of the cutting process. The specific form of the volume heat diffusion equation in the Lagrangian configuration applied to a 2D thermographic framework can be expressed as:

$$\underbrace{\boldsymbol{\rho}\mathbf{C_p}\left(\frac{\partial\bar{\theta}}{\partial t} + \vec{v}\cdot\vec{\nabla}\bar{\theta}\right) - k_1\left(\vec{\nabla}\bar{\theta}\right)^2 - \mathbf{k}\Delta_2\bar{\theta} + \frac{2h\theta}{e} + \frac{2\sigma\epsilon}{e}(\bar{T}^4 - T_r^4)}_{\text{Experimental evaluation}} = \underbrace{w'_{ch} = \beta(\sigma : \dot{\epsilon}_p)}_{\text{Numerical evaluation}} \quad (2)$$

where:

- $\bar{\theta} = \bar{T}(\mathbf{x}, \mathbf{t}) - T_0$ is the difference between the current and the initial temperature T_0.
- $\boldsymbol{\rho}\mathbf{C_p}\left(\frac{\partial\bar{\theta}}{\partial t} + v\nabla\bar{\theta}\right)$ is the intertial term that links the temperature evolution at a given location (**x, t**). Variable v stands for the velocity vector field.
- $k_1\left(\vec{\nabla}\bar{\theta}\right)^2 - \mathbf{k}\Delta_2\bar{\theta}$ is the diffusion (Laplace's) term. Note that∇ is the two dimensionnal gradient and Δ_2 the two-dimensionnal Laplace operator.
- $\frac{2h\theta}{e} + \frac{2\sigma\epsilon}{e}(T^4 - T_r^4)$ are the convective and radiative heat losses over the front and back faces of the sample. σ stands for the Stefan-Boltzman constant. h is the heat transfer coefficient chosen to be equal 50 W m^{-2} K^{-1}. T_r is the room temperature. However, this quantity has been assessed and compared to laplacian and inertial terms in previous work [49]. Accordingly, it was neglegted in the present analysis.
- $w'_{ch} = d_1 = \beta(\sigma : \dot{\epsilon}_p)$ is the heat source term and equals the intrinsic dissipation d_1 in absence of the thermoelastic couplings. β, σ, $\dot{\epsilon}_p$ are respectively the Taylor Quinney factor, the Cauchy stress tensor and the strain rate tensor.
- The material parameters are then $\boldsymbol{\rho} = \rho_1\theta + \rho_0$ the mass density, $\mathbf{C_p} = C_1\theta + C_0$ the specific heat, $\mathbf{k} = k_1\theta + k_0$ the thermal conductivity. According to [52,53], they were chosen to evolve linearly as a function of temperature (see Table 5).

Rather than temperature and kinematics fields analysis, the objective of the experimental part is to assess the left hand side terms from the measured quantities ($\bar{T}(\mathbf{x}, \mathbf{t})$ and T_0) in order to provide an estimation of the involved power in the cutting phenomenon w'_{ch}. It is then compared with the right hand side term which is evaluated numerically from the intrinsic dissipation d_1 (see Section 5.6).

Table 4
The number of the captured images for the analyzed segment chip.

	Number of images	
	IR	Visible
Test 1	5	58
Test 2	1	10
Test 3	6	62
Test 4	1	11

3. Experimental results

Only one segment is investigated form each captured video. For reading and comparison purpose, images are labelled by their number and the percentage of the segment formation. The first image (0%) being the image where the segment first touches the tool and the last image (100%) being the image exhibiting a displacement of 50 μm after the segment being fully formed. The Table 4 resume the number of images obtained for each test.

As mentioned in the previous work [49], only one thermal image is acquired during the process at 15 m/min. It corresponds to a 40% progression of the segment. Consequently, other thermal images from other measured segments which have, approximately, the same size were selected for the analysis. It should be mentioned that no important drift of the thermomechanical quantities was observed during the cut.

However, experimental investigations on the chip genesis lead to split the mechanism into three successive steps [3,19,20]. During the first stage (i.e. compression step), a high compression state on the material is induced by the tool and located around the cutting edge. The segment stores the elastic energy while plasticity develops in the primary shear zone. An out of plane swelling of the segment is clearly visible in this phase. The end of this stage is defined by the shear plane creation and the uprising of a micro crack at the tool tip. During the shear phase, the crack initiates at the tool tip and evolves inside the shear zone toward the free chip surface. Finally, the segment is fully formed and slips on both the cutting face and the next segment (to be formed). Simultaneously, the tool tip starts the compression phase of the next one. As depicted in Fig. 3 the classical steps of the chip formation were observed and analysed for each test.

Such graph resulting from a DIC analysis based on minor and major strains (not presented here) as detailed in [19,20]. It is clearly perceptible that the three successives sub-processes are highly influenced by the cutting conditions. Firstly, it can be pointed out that the compression phase is more important with a null rake angle. The long duration of the compression phase leads to a rapid shear phase and to a particular chip genesis way. Indeed, during the compression phase, the segment stores elastic energy which is then dissipated in the next stages. Hence, the longer the compression phase lasts the faster is the segment ejection (i.e. short shear and extraction phases).

The compression phase is also affected by the cutting velocity. As shown in the tests 1 and 3 ($Vc = 3$ m min^{-1}), this phase lasts longer than in the case of tests 2 and 4 ($Vc = 15$ m min^{-1}).

On the other hand, it can be seen that crack propagation is delayed when low cutting speed are involved. This observation brings to light the cutting velocity effect in the strain localization and thus on the crack propagation. The rake angle effect on the strain localization and crack propagation is clearly shown in the Fig. 3. A curved strain localization zone is always observed with a null rake angle whereas it is linear with a rake angle of 15°. This crack path transition from curved to linear may results from the shape of the triaxiality zone. As detailed in [19,20], a hydrostatic pressure zone is located at the tooltip which is higher (in terms of magnitude and geometry) in the case of null rake angle than the positive one (due to the additional compression induced by the rake

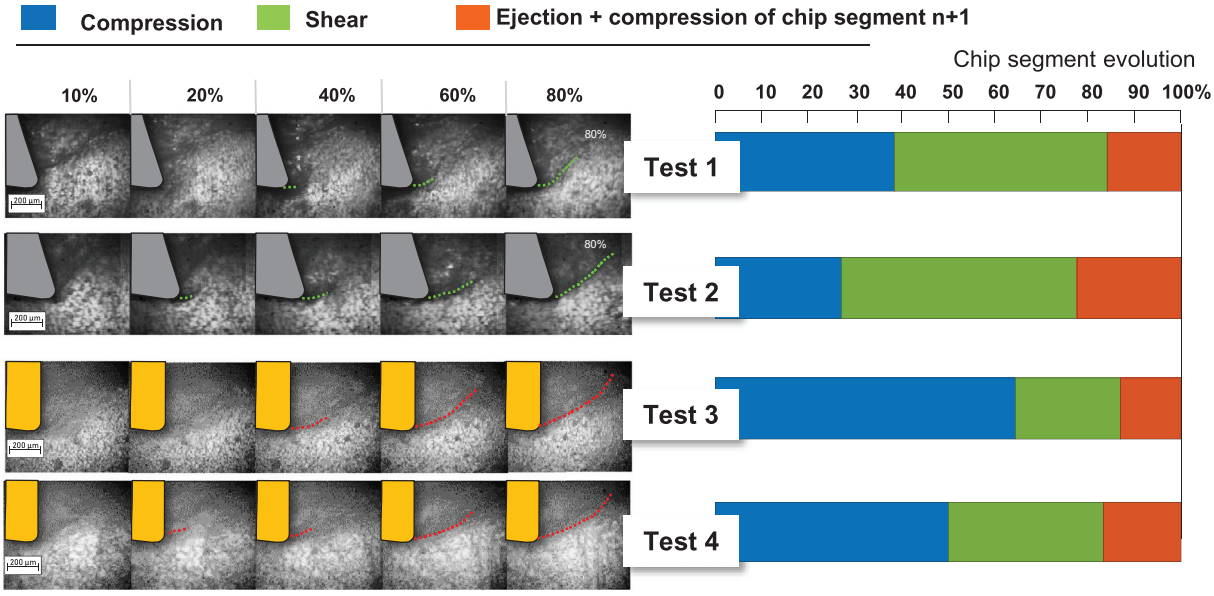

Fig. 3. 5 instant snapshot pictures acquired during the generation of one segment for the four investigated cutting conditions. The distinction between the three phases of the process relies on the crack propagation. The time elapsed in-between crack initiation and completion defines the shear phase.

angle). During the segment generation, the crack skirts the triaxiality zone in order to reach the free side surface. This latter being narrower for as the rake angle increase, the crack can reach the free surface in a straight manner. Consequently, the larger is the triaxiality zone the more curved is the crack path.

3.1. Kinematic fields

Fig. 4 presents the evolution of the logarithmic equivalent strain (a.k.a Hencky's strain) during chip segment formation. Strain localizations are clearly highlighted by significant strain magnitudes (up to 1.7). During compression phase, the strain magnitude is low and seems highly heterogeneous in space and in time. Then, the strain localization starts to move forward up to the shear plane creation. Finally, a straining band is observed which is fixed in space and only fluctuates in magnitude over time. The strain localization thickness is highly dependent on the cutting speed for both rake angles. It decreases as the cutting speed increases. This information proves that strain localization is mainly results from the cutting speed while strain magnitude is influenced primarily by the rake angle variation and at lesser scale by the cutting velocity. On the other hand, it can be noticed that the chip bulk (i.e. the side surface of the chip which located away from the first and second shear zones) is not significantly deformed when the cutting speed varies. Conversely, it seems to be influenced by the variation of the rake angle.

The strain rates are also greatly influenced by the cutting speed. A high strain rates magnitude is observed for early stage of the segment chip formation ($\sim$ 20%). This phenomenon plays a lead role for strain localization and crack propagation since the equivalent strain at failure decreases at high cutting speed. Consequently, it leads to a rapid segment chip formation. However, the rake angle influence on the strain rate is not negligible [19,49]. A drop of 50% in the strain rate is observed at low cutting velocity. Conversely, this effect is not observed at 15 m min^{-1} where a comparable magnitude is obtained.

3.2. Thermal fields

Fig. 5 depicts the temperature and intrinsic dissipation distributions during chip segment formation. The temperature increases with the cutting velocity augmentation and at a lesser scale with the rake angle diminution.

At low cutting speed and using a 0° rake angle, no clear localization is found before 60% of segment formation. However, by varying the rake angle to 15°, an earlier temperature localization is observed (i.e. at 40% of the segment formation). For all tests, the maximum temperature does not evolve significantly during the sequence, only ranging from 590 K to 633 K. However, the temperature gradient is significant in space. The min/max range within the same image is around 573 K mm^{-1}. Indeed, the main temperature rise seems to occur during the transit of a material point through the primary shear zone. It also should be mentioned that the maximum temperature location is located in the primary shear zone (ZI). Such findings lead to consider that heat generated in ZI (from plasticity and damage) is more important than in the secondary and tertiary shear zones where friction is often assumed to play a leading role. It can be explained by the short period of machining ($\sim$ 1.2 s) which corresponds to a transitional stage. It is worth reminding that only a small part of the secondary shear zone is captured by the thermal camera during the process. Indeed, further investigations with a thermal image of the whole scene of cut need to be conducted to be conclusive on this matter.

Conversely to temperature, a localization of the intrinsic dissipation is observed at early stage of chip segment formation. Such effect is detected especially at high cutting speed. The dissipated power evolution can be described through three stages: at first $\sim$ 20%, the dissipated power is low and is concentrated at the tool tip. Then, from a progression in-between $\sim$ 20% to $\sim$ 60%, the dissipated power increases and moves toward the middle of the primary shear zone. During the final stage of the segment chip formation, it is seen from the latest images that even while the crack propagation is completed, and that strain accumulation stalls, the generated power remains high. The thermal source magnitude increases by 43% when multiplying by 5 the cutting speed and a small reduction is observed by varying the rake angle to 0°. These observations seem not surprising considering the high localization observed with a rake angle of 15° and especially at high cutting speed. In addition, it is clearly perceptible that the additional compression induced by the null rake angle disrupts the shear mechanisms and consequently the localization phenomena. The heat source in this case seems more important in the space but with a smaller magnitude than in the case of tests 1 and 2.

It should be mentioned that the generation of segment n overlaps with the one generation $n-1$. It is visible from Fig. 5 at 10% (for all

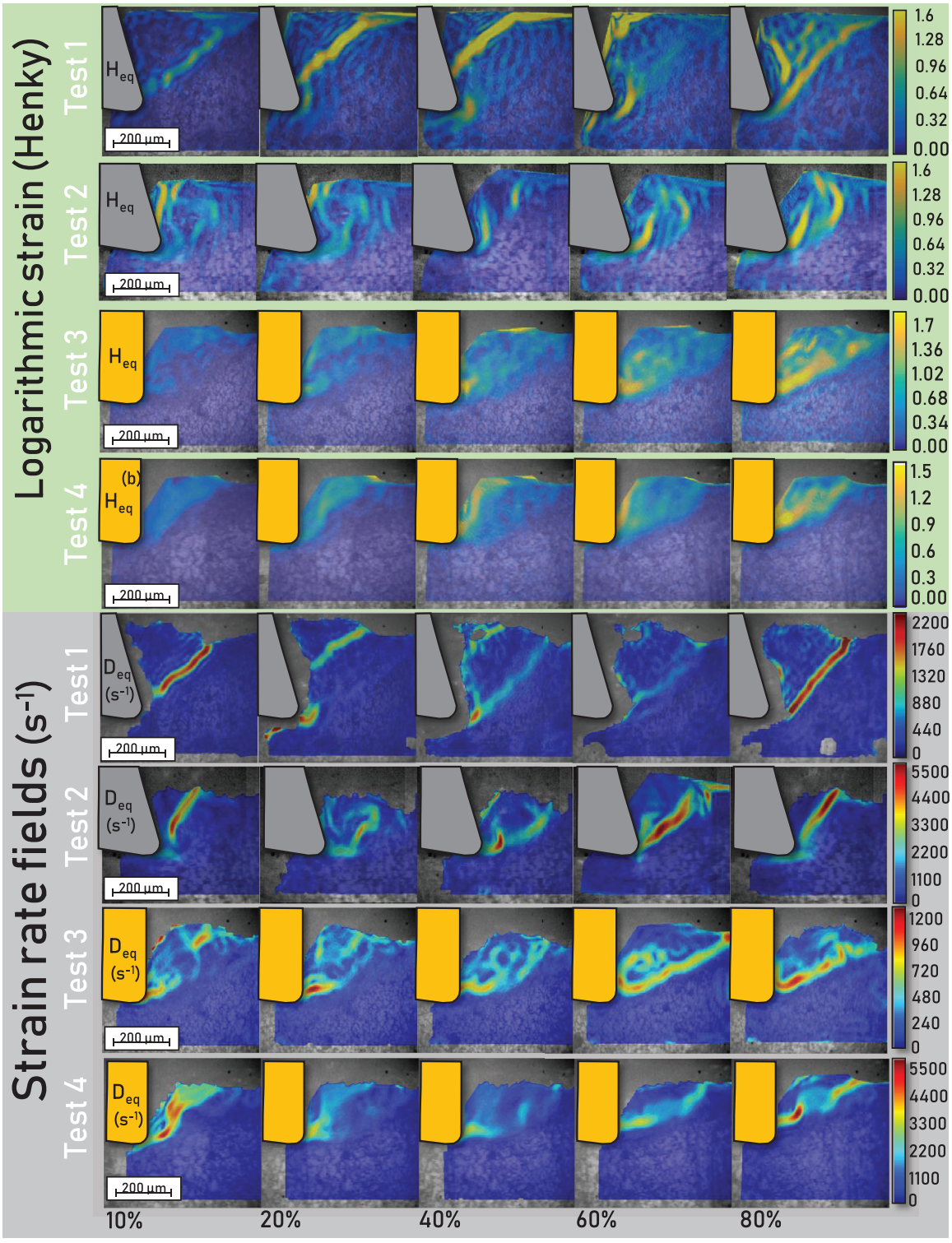

Fig. 4. 5 instant images of the strain and strain-rate fields distributions during the generation process of one single segment. The four cutting conditions under investigation are depicted (3 m/min – 15 m/min and 0° – 15°).

machining condition) that two heat sources are active simultaneously : the upper one corresponding to the sliding of segment $n-1$ and slightly beaneath the dissipation due to the early stage of compression in segment n. the input mechanical power is split in two locations, the first consists in the sliding of the segment n-1 over the segment n and the second is the early stage of generating segment n.

The previous experimental section brings to light the thermomechanical aspect of the Ti-6Al-4V chip formation. The kinematics and thermal fields evolutions are presented and discussed. The strain localization phenomenon plays an important role in the shear plane creation. Its magnitude is mainly piloted by the cutting velocity and its shape is strongly related to the cutting geometry (i.e. the rake angle and feed).

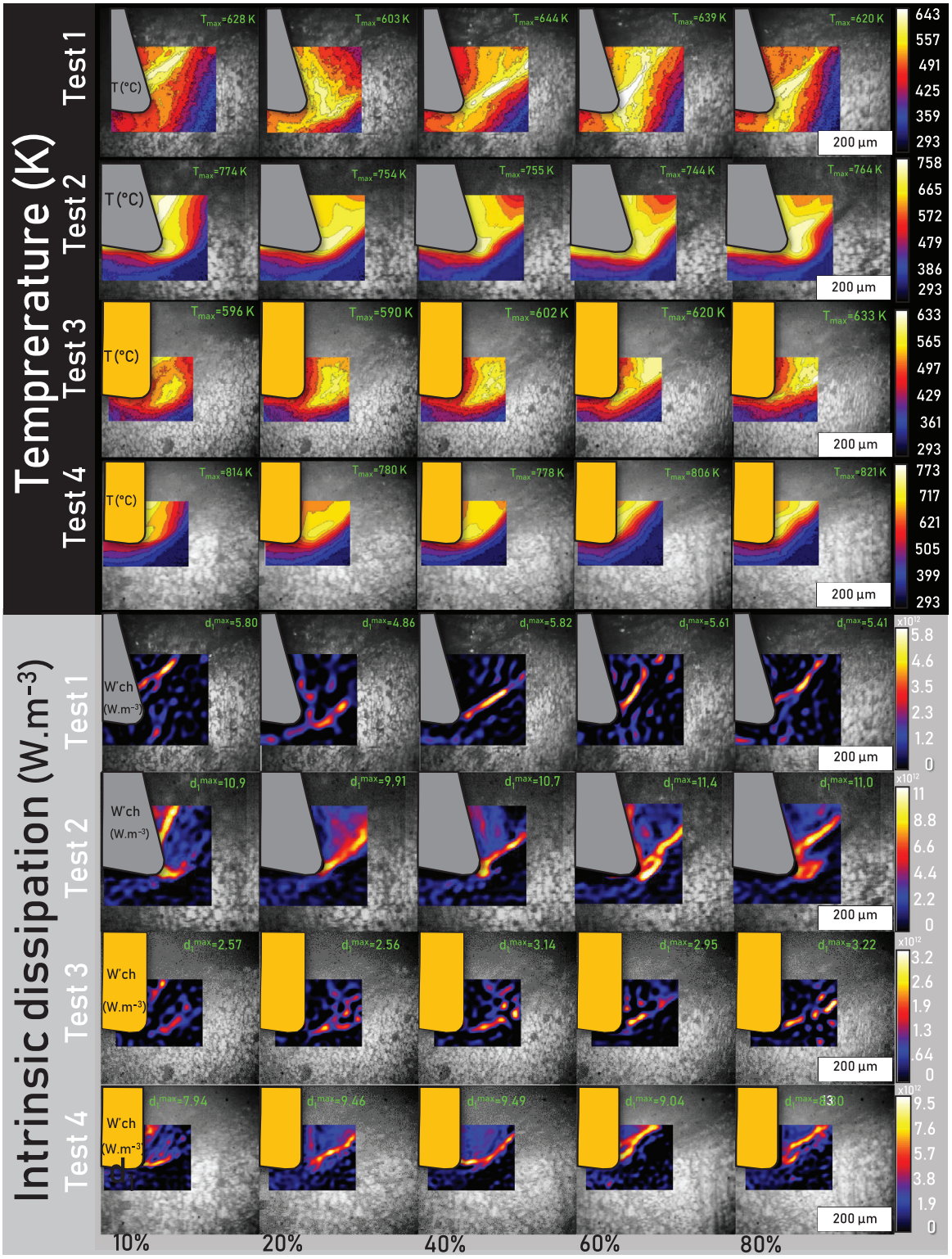

Fig. 5. 5 instant images of the temperature and intrinsic dissipation distributions during the generation process of one single segment. The four cutting conditions under investigation are depicted (3 m/min – 15 m/min and 0° – 15°).

From a thermal stand point, the maximum temperature is usually located in the primary shear zone. Its magnitude is mainly influenced by the cutting speed and at a lesser scale by the rake angle. By highlighting both Figs. 4 and 5, one can therefore prove that the equivalent strain at failure is smaller at high cutting speed even though the temperature in the primary shear zone is higher. This result testifies the loss of ductility of material following a competition with the strain softening in this range of thermomechanical loading.

The specific power is also influenced by the machining parameters. The thin straining band induced at high cutting speed leads to a high concentration of the intrinsic dissipation. However, the dissipation in the segment bulk and in the sub-surface is far from negligible. Further

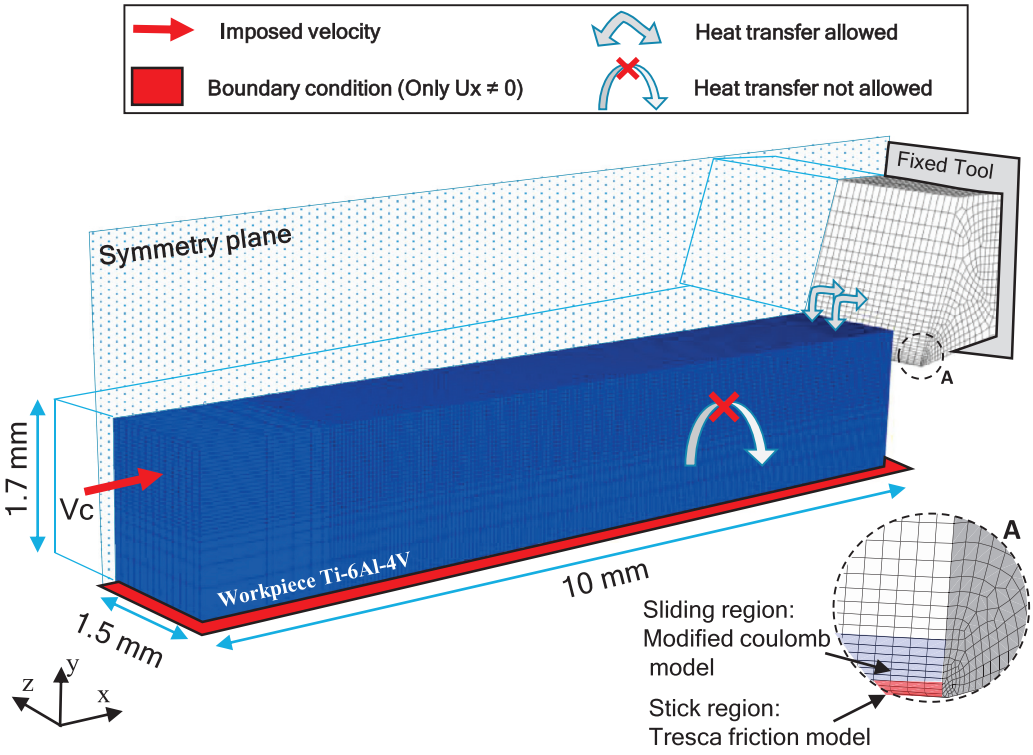

Fig. 6. Geometry and boundary conditions used for the implementation of a 3D FE orthogonal cutting model.

investigations are required to link this phenomenon to the surface integrity (i.e. residual stresses, ...) of the generated surface.

4. Numerical approach

4.1. 3D geometric finite-element (FE) model, boundary conditions and mesh sensitivity

The 3D geometric model proposed consists in a carbide cutting tool and a part made of Titanium alloy Ti-6Al-4V. The workpiece to machine is modelled as a parallelepiped measuring 10 mm in length, 1.7 mm in height and 1.5 mm in width ($w = 3$ mm but a plane of symmetry is defined). It was created by a single part in order to respect the physical phenomena in order to avoid many modeling hypotheses. The tool geometry and the cutting conditions are the same as for the experimental study.

As detailed in Fig. 6, the 3D finite element model is created under symmetric condition in order to investigate the evolution of the chip mechanism either under plane strain assumption (center of the chip $z = w/2$) and plane stress assumption (side free surface $z = 0$). The back surface of the tool is locked over 6 dof. The bottom surface of the workpiece is only free to translate along the X axis. The displacement of the nodes on the back surface of the workpiece is imposed with a constant velocity that equals the desired cutting speed. However, heat transfer is allowed only between the two parts.

3D continuum elements under reduced integration (C3D8RT) were adopted for thermomechanical fields calculation. Regarding the hourglass control, a relax stiffness method is used to prevent hourglassing as recommended by Barge et al. [54].

To make a compromise between both computing cost and accuracy, a mesh sensitivity analysis is computed using an iterative method. Accordingly, a series of simulations are carried out by varying the characteristic length of element (L) from 55 μm to 5 μm with an incerement of 5 μm. For each simulation, both average and maximum of the cutting forces (x direction) are recorded for the error calculation. Hence, the error is calculated between two successives mesh size (i.e. i and $i-1$) as follows :

$$Mesh\ error_i\ (\%) = \sqrt{\left(\frac{average(Fc)_i - average(Fc)_{i-1}}{max(Fc)_i}\right)^2} \times 100 \quad where\ i = 0\ to\ 10 \tag{3}$$

As depicted in Fig. 7, the error seems to be stable from 25 μm of the mesh length for a computing time of 3 h and 37 min. In addition, the chip formation shows that from this value of the characteristic mesh length can well capture the shear localization and the crack propagation on the chip. Consequently, the mesh size $25 \times 25 \times 115$ μm^3 was chosen in the region of interest and beyond this zone a coarsest mesh is adopted which is ranges in-between ($200 \times 300 \times 115 - 500 \times 300 \times 115$ μm^3).

4.2. Material constitutive and damage laws

The mechanical behavior of the carbide tool is modelled by a classical thermo-elastic law. The mechanical parameters of the workpiece and the carbide tool (WC) are given in Table 5.

Since the tight coupling between phenomena (mainly between temperature and strain rate) that occurs during the chip formation, the mastery of workpiece behavior and damage evolution is essential. Therefore, the workpiece behavior is modelled by a modified Ludwick law undertaking a tight coupling between temperature and strain rate. This model is presented in the Eq. (4) of the equivalent plastic flow stress.

$$\sigma = A(\dot{\varepsilon}, T) + B(\dot{\varepsilon}, T).\varepsilon^{n(\dot{\varepsilon},T)} \tag{4}$$

where $A(\dot{\varepsilon}, T)$, $B(\dot{\varepsilon}, T)$, $n(\dot{\varepsilon}, T)$ are respectively the yield strength, the hardening modulus and the hardening coefficient and exhibit a dependency on both the strain rate and temperature. However, the evolutions of each parameter according to these two quantities were described by a bilinear interpolation as detailed in a previous work [20].

The damage modeling classically relies on a cumulative formulation of the damage internal variable D, of which the evolution throughout

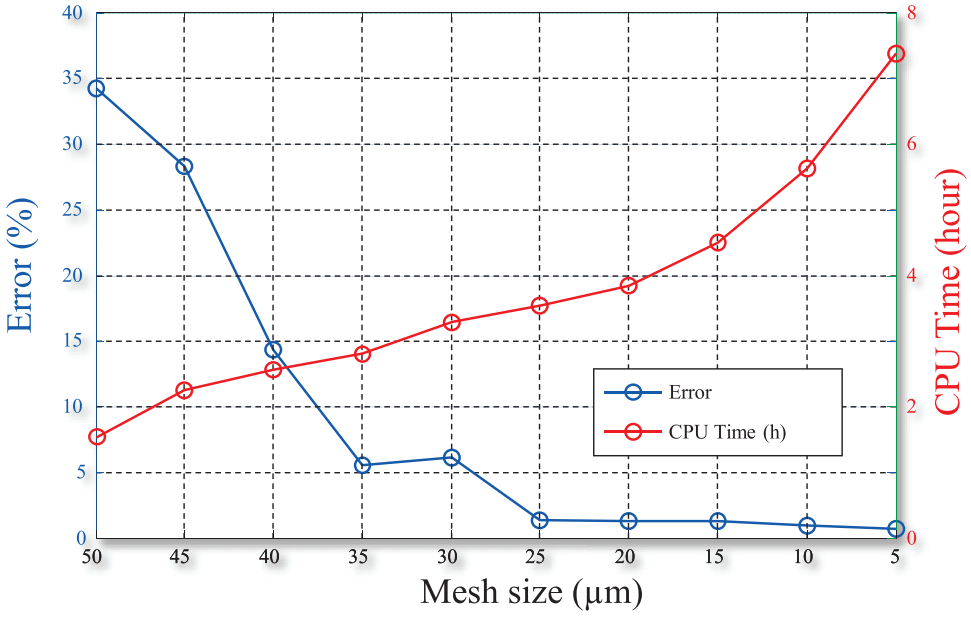

Fig. 7. Mesh size sensitivity analysis. Depiction of the evolutions of : (i) the error on the global cutting force and (ii) the CPU time, as a function of the mesh size. (CPU characteristics: AMD opteron 6376 / 2 processors 16 Cores/ 2.3 GHZ /RAM 132 Go).

Table 5
Mechanical and thermal properties of the carbide tool and Ti-6Al-4V workpiece (20 °C – 550 °C) [6,52,53].

Properties	Material	
	Ti-6Al-4V	WC
Young modulus E (GPa)	$118.8 - 0.09.T$	705
Density ρ(kg m^{-3})	$4452 - 0.1T$	15,700
Poisson's ratio ϑ	0.33	0.23
Specific heat $C_p\left(\mathrm{J}\ {}^{-1}\mathrm{K}^{-1}\right)$	$552.8 + 0.358.T$	$-2.10^{-4}.T^2 + 0.313.T + 220$
Thermal conductivity k(W m$^{-1}K^{-1}$)	$6.58 + 0.0057.T$	$-8.10^{-5}.T^2 + 0.07.T + 43.1$
Expansion Coefficient $\alpha_d\left(\mathrm{K}^{-1}\right)$	1.15^{-5}	5.10^{-6}
Room temperature T_r (K)	293	293
Fusion temperature T_f (K)	1903	–
Taylor-Quinney coefficient	0.8	–

plasticity is defined as a function of the increment of plastic strain $d\varepsilon_p$ by:

$$\dot{D} = \frac{d\varepsilon_p}{\bar{\varepsilon}_f} \tag{5}$$

Such formalism requires a good assessment of the strain at failure $\bar{\varepsilon}_f$. In fact, the shear nature of the mechanism and the narrow range of stress triaxiality η involved in cutting $(approximately - 0.33 < \eta < 0.33)$ have led to consider max shear failure criterion as well suited for this investigation [20]. This law can be described as a function of the normalized Lode angle $\bar{\theta}$ by Eq. (6).

$$\bar{\varepsilon}_f = \left[\frac{\sqrt{3}\tau_f(\dot{\varepsilon},T)}{B(\dot{\varepsilon},T)cos\left(\frac{\pi\bar{\theta}}{6}\right)} - \frac{A(\dot{\varepsilon},T)}{B(\dot{\varepsilon},T)}\right]^{\frac{-1}{n(\dot{\varepsilon},T)}} \tag{6}$$

The strain rate and temperature dependency is thus addressed through the material parameters and the maximum shear stress at failure $\tau_f(\dot{\varepsilon},T)$. The latter is the only parameter to calibrate and is described as a function of temperature and strain rate by a bilinear interpolation as detailed in [20]. The plane equation is recalled in Eq. (7) whereas the parameters values used in simulations are specified in Table 6. It is important to note that the damage and behavior laws are successfully implemented in the FE model by means of VUMAT subroutine.

$$A, B, n, \tau_f = -a.T - b.ln\left(\dot{\varepsilon_p}\right) - c \tag{7}$$

Table 6
Behavior and damage law parameters [20].

	A (Pa)	B (Pa)	n	τ_f (Pa)
a	$9.36e+005$	$5.57e+05$	$9.46e-05$	$7.1716e+05$
b	$-1.45e+08$	$4.66e+07$	$4.23e-02$	$9.3088e+07$
c	$-8.65e+08$	$-6.39e+08$	-0.365	$6.9573e+08$

4.3. Contact conditions and friction modeling

In addition to behavior and damage laws, the simulation of the chip formation process also requires a good description of the interaction between the tool and workpiece. Therefore, a particular attention is paid to the friction model. As proved by several authors, the tool/chip interface can be divided in two distinct regions where the tribological behavior is clearly different [55–57]. The first region (i.e. stick region) is located around the tool tip and is characterized by a strong material adhesion due to high contact pressure. The second region (i.e. slip region) is characterized by a sliding motion of the chip along the rake face.

In the present study, a new stick-slip friction model is proposed as formulated in Eq. (8) and described in Fig. 6 (detail A). Accordingly, the stick region was described by a Tresca friction law with a coefficient value m_k equal to the unity [27]. On the other hand, the sliding region is modelled by a modified Coulomb friction law which friction parameter μ is described as a function of the sliding velocity V_{sl} as proposed in [58]. σ_n and τ represent respectively the normal and shear friction

stresses.

$$\begin{cases} |\tau| = -m_k \cdot \frac{\sigma_n}{\sqrt{3}} \cdot \frac{\overrightarrow{V_{sl}}}{||\overrightarrow{V_{sl}}||} : \text{Tresca friction law (for stick region)} \\ |\tau| = -\mu(V_{sl}) \cdot \sigma_n \cdot \frac{\overrightarrow{V_{sl}}}{||\overrightarrow{V_{sl}}||} : \text{Modified Coulomb friction law (for sliding region)} \end{cases} \quad (8)$$

As pointed out by Bodwen and Tabor [59], the apparent friction parameter results from two contributions. It includes on one hand the adhesive phenomena, that are affected by the material properties such as hardness, asperities, and on the other hand the plastic deformation of the workmaterial, which cannot be neglected under such severe contact conditions. Based on this consideration, several studies proved that the adhesive part of the apparent friction parameter is close to 90% in the case of titanium alloy Ti-6Al-4V [58,60]. Accordingly, only the adhesive part is introduced in simulations. The friction law is successfully implemented in the numerical model through Vfric user subroutine.

Another important feature of the model is the heat partition coefficient β_p. It defines the ratio of the friction thermal power that spreads within the tool T (and thus $1-\beta_p$ within the workpiece W). Several models have proposed different approaches in the assessment of such coefficient [61,62]. The most recent approaches relies on the Thermal Contact Resistance (TCR) which assessment is a dedicated experimental challenge in its own right [63,64]. In the present work, the original approach proposed by Blok [61] and Jaeger [62] has been chosen. This latter does not require the evaluation of the TCR but rather defines β_p as a ratio of thermal effusivites of the tool ζ_T and workpiece ζ_W in the case of a dynamic contact. Such definition has already been successfully implement in the fields of cutting simulation [3,38] and reads :

$$\beta_p = \frac{\zeta_T}{\zeta_T + \zeta_W \times \sqrt{Pe}}$$

$$\text{where } \zeta_i = \sqrt{\rho_i . Cp_i . k_i} \text{ and } P_e = \frac{L \times V_s \times \rho_W \times Cp_W}{4 \times k_W} \quad i = T, W \quad (9)$$

where, Pe is the Peclet number, V_s the sliding velocity and L the contact width. The evaluation of the Peclet number requires the input of the sliding velocity which is an experimental blind spot. Accordingly, four values of β_p was calculated: at $(20\,°C/3\,m\,min^{-1}, 500\,°C/3\,m\,min^{-1}; 20\,°C/15\,m\,min^{-1}, 500\,°C/15\,m\,min^{-1})$. The material parameters for Tungsten Carbide and Ti-6Al-4V were those of Table 5. The obtained values (0.58, 0.56, 0.75, 0.74) was averaged to obtain a value of $\beta_p = 0.66$ which was set in the model. Its should be mentioned that 90% of the plastic work induced by frictions phenomena is converted into heat [3,20].

5. Numerical and experimental confrontation

The use of coupled measurement and FE simulations constitutes a powerful tool for investigations and provides a precious insight of chips generation phenomenon from which some conclusions can be drawn but it also brings many subsequent questions. The present section deals with the numerical and experimental results obtained from orthogonal cutting of titanium alloy Ti-6Al-4V. The comparison between the two approaches is performed through several aspects. Accordingly, the relative error is calculated as described in Eq. (10).

$$Error(\%) = \sqrt{\left(\frac{max(Output_{num}) - max(Output_{exp})}{max(Output_{exp})}\right)^2} \times 100 \quad (10)$$

The chip morphology is discussed and cutting forces are thus monitored and compared. Moreover, a particular attention is paid to the thermal aspect in terms temperature evolution and intrinsic dissipation during the chip generation.

5.1. Chip morphology

Fig. 8 depicts the numerical chip morpholgy as well as the damage fields obtained for the four machining conditions. All the performed cutting tests led to serrated chips, generated from quasi-periodic cracks propagation. Chips segments are separated by damaged zones which emphasize the magnitude of the thermo-mechanical loadings and cracks propagations history induced during the process. The crack initiates at the side free surface, close to the tool tip and propagates within the material.

The classical dependency between the cutting speed and the chip size is also found. The chip size decreases as the cutting speed rises

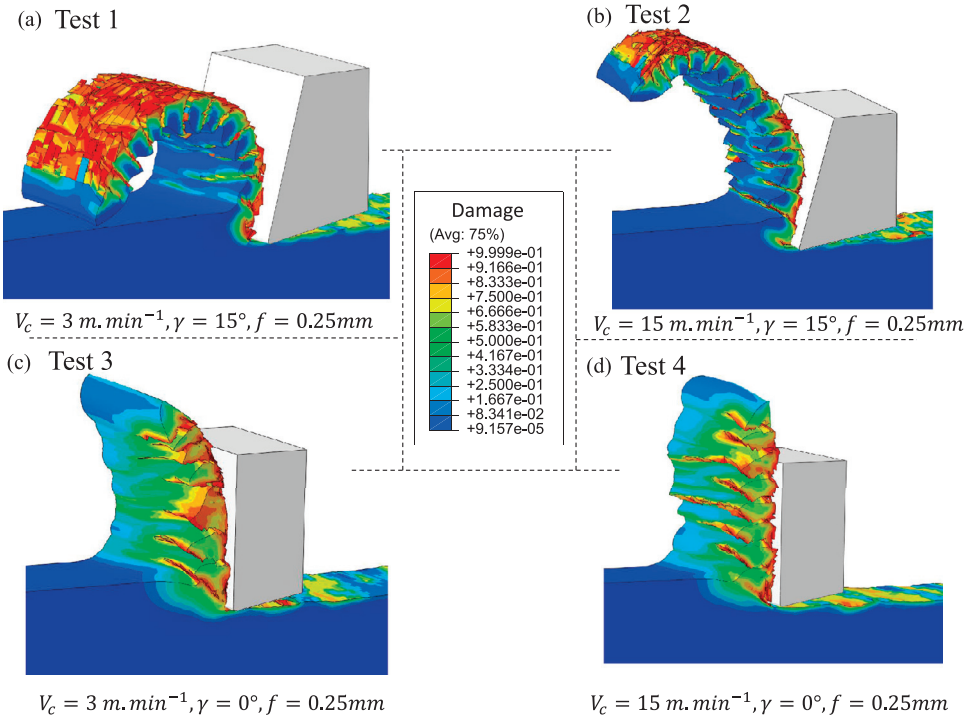

Fig. 8. Chip morphologies obtained from the FE model for the four cutting conditions.

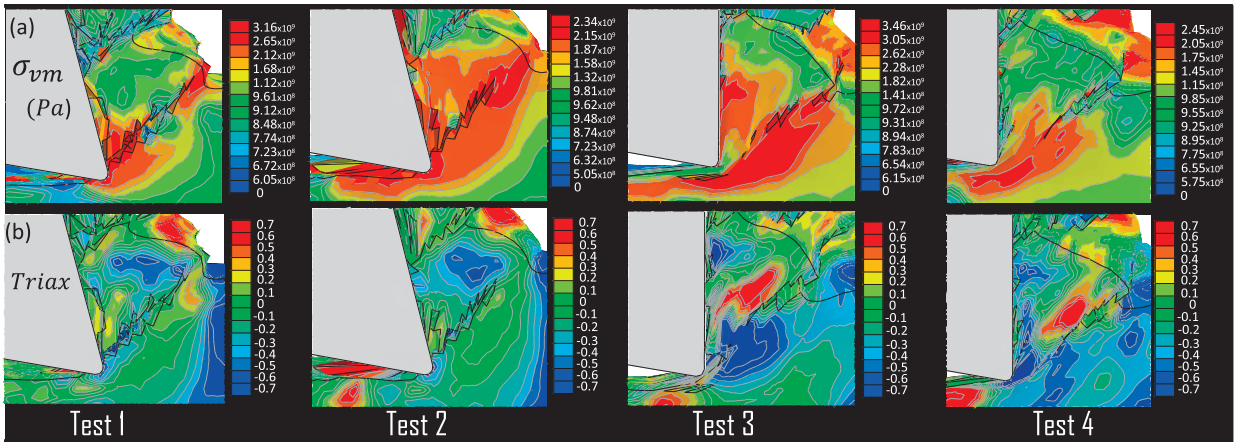

Fig. 9. Numerical vonMises stress and stress triaxiality fields for the different machining conditions at 80% of the segment formation.

Table 7
Mean values and errors of experimental and numerical forces under all machining conditions.

	γ (°)	feed (mm)	Vc (m min^{-1})	$Fc_{\exp}$ Average	Fc_{num} Average	Fc error %	$Ff_{\exp}$ Average	Ff_{num} Average	Ff error %
Test 1	15	0.25	3	1463	1329	9.15	693	627	9.52
Test 2			15	1233	1153	6.48	512	473	7.61
Test 3	0		3	1611	1528	5.15	789	733	7.09
Test 4			15	1516	1435	5.34	745	689	7.51

higher resulting an important number of chip segments. It should be mentioned that a significant transversal deformation of the chip surface (out of plane) is observed for all cutting conditions. As proved by several authors, this latter phenomenon seems affected mainly by the rake angle and at a lesser scale by the cutting speed [19,20,49].

Damage is mainly concentrated in the primary and secondary shear zones. Thin bands are observed in the case of tests performed with positive rake angle and specially at 15 $m.min^{-1}$. In the case of third and fourth tests, a higher magnitude of damage is observed in the chip bulk. As illustrated by Fig. 9a, the use of a null rake angle gives birth to an additional stress in the chip segment during the process which induces deformation of the chip bulk and creation of a strong hydrostatic compressive zone at the tool tip.

Fig. 9 b, shows the computed stress triaxiality (triax) at 80% of the chip evolution for different cutting conditions. It can be seen that the mechanical loadings differ with the rake angle changes. For a positive rake angle, it is clearly found that shear is the leading mode of failure. However, a compressive/shear state is noticeable in the case of the third and fourth tests. Due to this effect, the numerical material elements are highly deformed and stacked therefore removing a significant part of the depicted crack path line. A hydrostatic compressive zone is observed nearby the tool tip. Its shape and magnitude seems strongly affected by the rake angle and at a lesser scale by the cutting speed. Based on these observations, it appears that the shape of the shear plane mainly results from the shape of the hydrostatic compressive zone. In the case of the first and the second tests, a simple and linear evolution of the crack propagation path is observed. By contrast, a curved crack path shape is found in the case of tests 3 and 4. Accordingly, the crack propagation seems to avoid the hydrostatic compressive zone in order to reach the free side of material. These numerical observations are very similar to the experimental ones. In addition, it justifies the particular chip shape found with null rake angle and brings to light several challenges about the influence of the hydrostatic pressure on the shape and geometry of the shear band especially, in the case of anisotropic materials where the relation between stress and strain triaxiality is no longer straight forward.

5.2. Cutting forces

As mentioned in the above cutting forces are measured through 6-components dynamometer (Kistler 9257A). Unfortunately, its natural frequency (7 kHz) is too low in comparison with chip formation frequency. In addition, the generation of segment n partially overlap in time by the generation of segments $n-1$ and $n+1$. This justifies the difficulty in post-processing macroscopic forces using such device. Consequently, only averages of the cutting and feed forces are considered and compared as detailed in Table 7.

It can be noted that both cutting and feed forces are affected mainly by the rake angle and the cutting velocity. It increases by varying the rake angle toward null value or by decreasing the cutting velocity. Regarding this issue, the 3D numerical model presents a good agreement with an acceptable error. However, the numerical forces are underestimated in all simulated cases. In addition, the error seems to be more meaningful in the case of the feed force and specially for the test 1. This underestimation can be originating from many sources. In fact, the contact conditions are highly influenced by the rake angle variation which is not taken into account in this FE model. In addition, the use of the element deletion method, the assumption of a constant cutting velocity, and the chosen mesh size can also be the origin of the obtained error. On the other hand the computed cutting forces provide a better match of the experimental ones when the rake angle equals 0°.

5.3. Logarithmic strain (Heq)

Fig. 10 a and b allow the comparison between numerical and experimental strains in the chip segment. Over all tests, the numerical logarithmic strain seems underestimated. Event though the error is small for tests 3 and 4 ($\sim$ 10%), it is more pronounced in the case of positive rake angle ($\sim$ 24%). This error can be mainly attributed to the simulation technique. Since the eroding element technique is employed in FE simulations, the strain highest cumulation is discarded along with its bearing element. As depicted in Fig. 10c, a good agreement between numerical and experimental strain paths is observed. By contrast, a part of

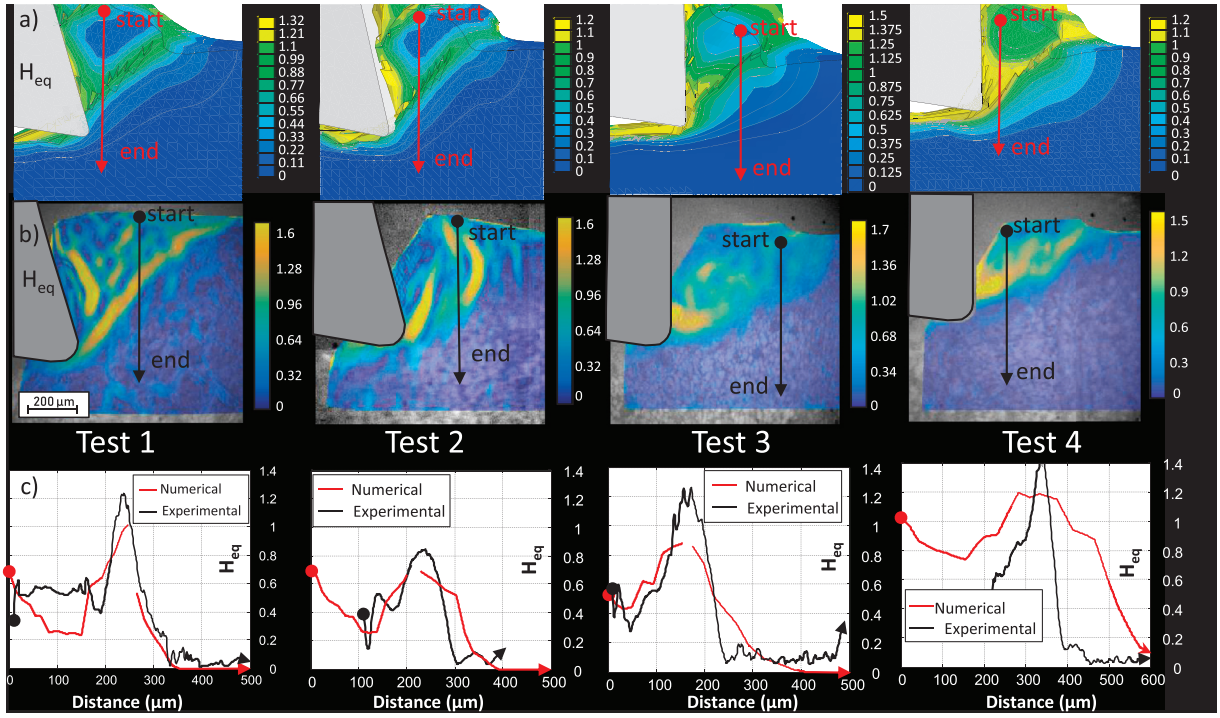

Fig. 10. Numerical and experimental distributions of the logarithmic strain fields: Comparisons at 80% of the segment formation and for all tests. (a) Numerical distribution of the logarithmic strain (b) Experimental distribution of the logarithmic strain (c) Logarithmic strain paths extracted from the numerical and experimental results (see the arrows directions). The numerical strain peaks are eroded by the numerical element deletion technique.

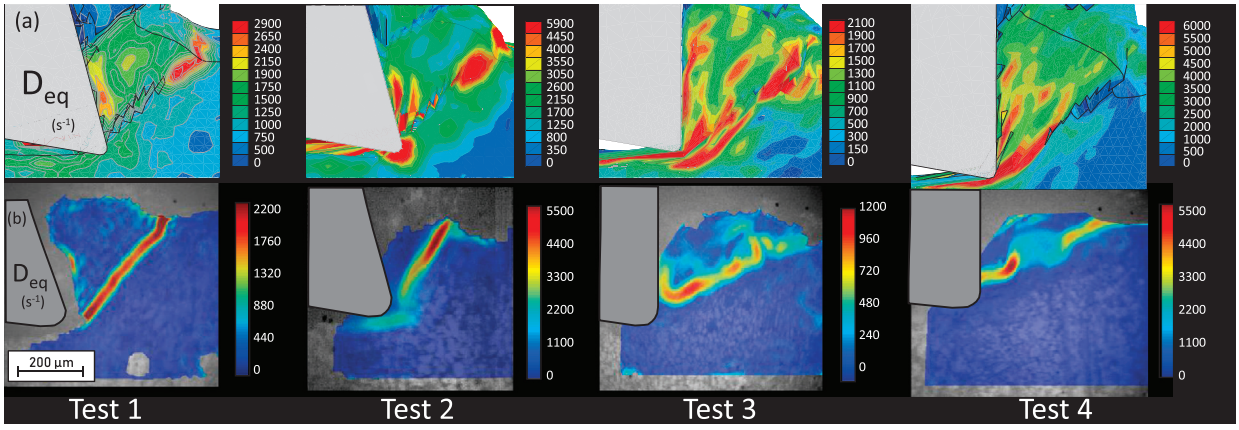

Fig. 11. Numerical and experimental distributions of the strain rate fields: comparisons at 80% of the segment formation and for all tests: a) numerical results b) experimental results.

the numerical response is not found. This finding leads to consider that the numerical peaks are removed by the erosion element technique. Despite the numerical artifact, the FE model presents a good sensitivity on the logarithmic strain as a function of the cutting conditions. Alike the experimental observations, the model predicts that the strain magnitude decreases by varying the rake angle from 0° to 15°.

5.4. Strain rate (Deq)

Numerical and experimental strain rate fields at 80% of the chip segment formation are depicted in Fig. 11. The high magnitude of the strain rate is located mainly in the primary and secondary shear zones. Although the spatial evolution of the strain rate is correctly predicted by FE numerical model, an overestimation is noted over all tests and especially for test 3.

This error can be induced by the friction model. Since the friction model is composed by two distinct regions, the limit in between these latters is arbitrarily selected. Consequently, the plastic strain and strain rate induced by friction at the tool tip and in the secondary shear zone seem influenced by this arbitrary zone distinction. This point is therefore a clear perspective of the present work. As declared in [49], the VISIR device is focused mainly in the primary shear zone. Accordingly, the secondary shear zone is not bring to the fore in the present paper.

However, it is worth noticing that the FE and experimental shear angle bands are different. This difference can be explained by the complex path of the crack which is not retranscribed properly by the FE model. In fact, the use of element deletion induces variations on the shear angle and thus, on the kinematic fields evolution.

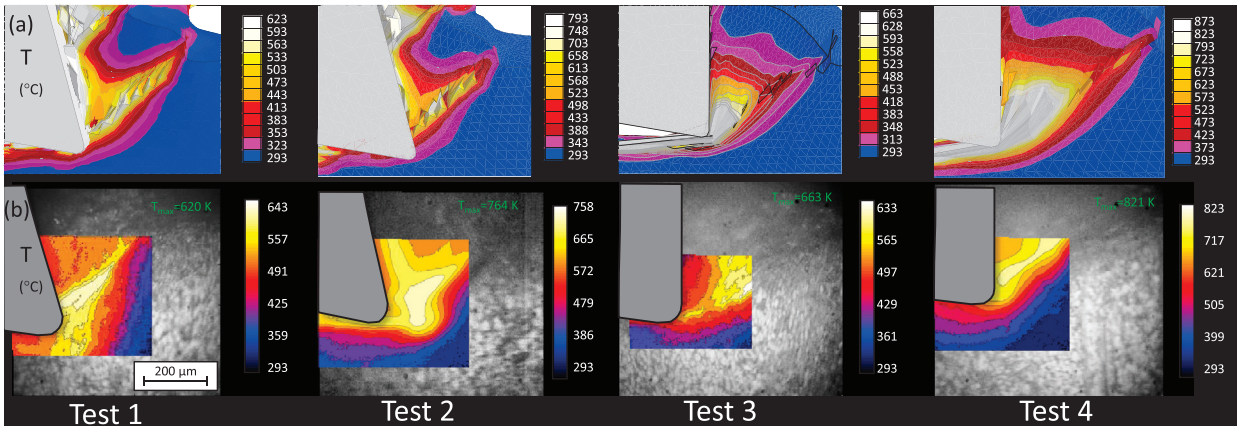

Fig. 12. Numerical and experimental distribution of the temperature fields at 80% of the segment formation and for all tests: a) numerical thermal fields b) experimental thermal fields.

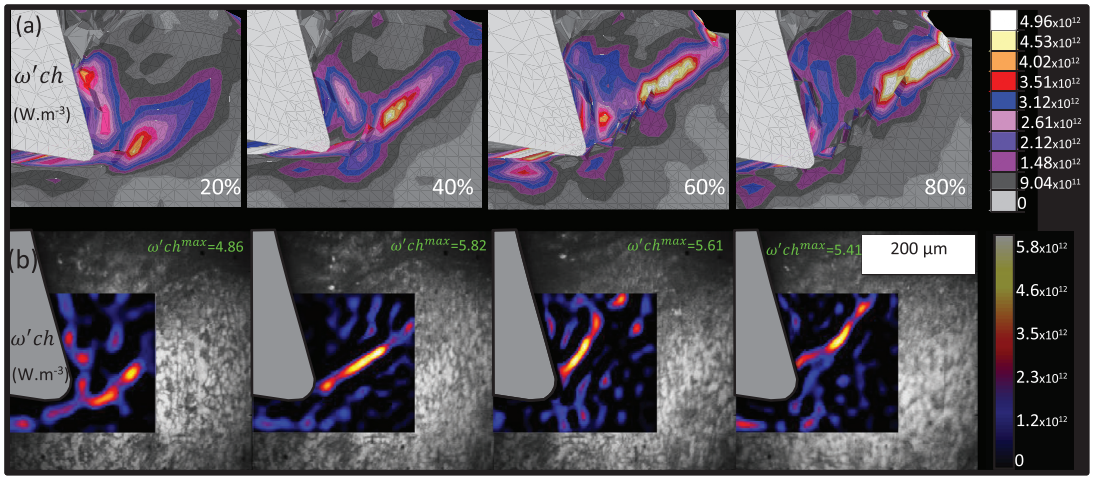

Fig. 13. The evolution of the intrinsic dissipation during chip segment formation in the case of Test 1. (a) numerical results (b) experimental results.

5.5. *Temperature T*

Numerical and experimental temperature fields are presented in Fig. 12. Overall, the experimental temperature seems correctly estimated under a relative error inferior to 12%. Experimentally, it can be seen that the maximal temperature is always located in the primary shear zone. By contrast, the numerical maximal temperature is mainly localized in both primary and secondary shear zones. This observation (along with the previous statement concerning the strain rates) shows that the chosen modeling of the tribological interface, although improving the segmentation quality, generates many errors in the kinematic and thermal fields.

Consequently, this latter point leads to consider that the tribological behavior requires a rigorous characterization and identification in terms of friction and heat partitions models for better modeling the chip-tool interface.

5.6. *Thermal dissipation*

The intrinsic dissipation stays the principal factor for temperature rise during machining. This phenomenon is analyzed and compared by two strategies as mentioned above in Eq. (2).

Fig. 13 prompts the experimental and numerical intrinsic dissipation evolution during chip segment formation. Despite the small overestimation in the secondary shear zone, the experimental distribution of this phenomenon seems correctly predicted by the numerical simulation. The dissipation initiates at the tool tip vicinity and moves in the straining band towards the free surface. For each segment formation step, a peak of thermal dissipation is observed which is followed by crack propagation. This findings tend to prove that the thermal dissipation is not induced only by the plastic deformation and the friction phenomena but also by the failure phenomenon [65–67].

As depicted in Fig. 14, the thermal dissipation magnitude is explicitly related to machining conditions. A small increase of the dissipation magnitude by varying the rake angle to 0° is noticed. In addition, the chip bulk seems deeply affected by the angle variation where some dissipation zones are observed. With the increase of the cutting speed (tests 2 and 4), a high elevation of the intrinsic dissipation is noted with a small dissipation distribution in the chip bulk. This constatation proves that the cutting velocity is the key driver for the strain localization. It's worth mentioning that the kinematic and thermal fields analysis was focused only on the plan of the captured images and thus, the internal strain was not analyzed in this study.

6. FE model contribution to the surface integrity on the final part

Among the aims of this contribution is the understanding of the physical phenomena inducing the segmented chip during machining. For that, experimental and numerical investigations of the kinematics and thermal fields were performed in order to achieve this goal.

However, the chip formation mechanism analysis in itself is not the final goal, but it's an unavoidable strategy toward better understand-

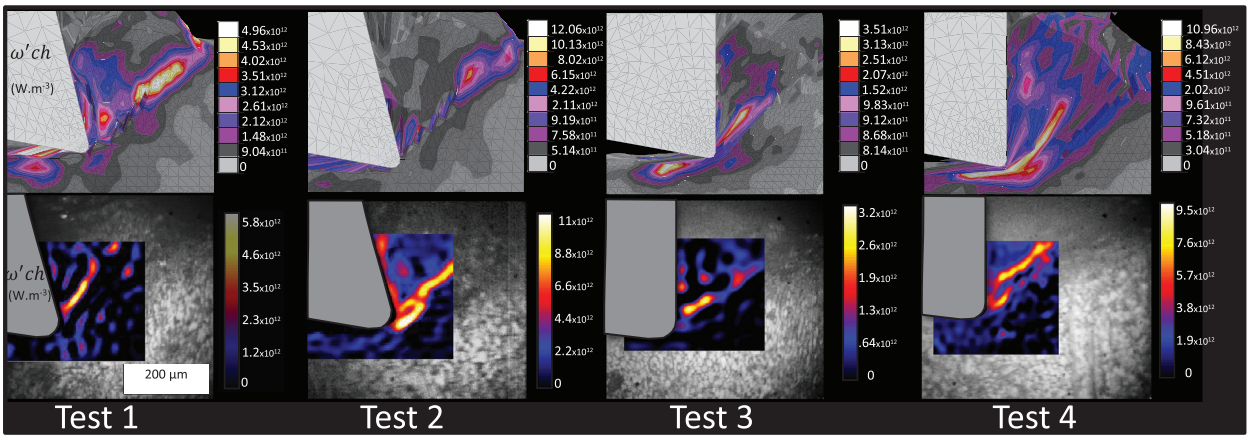

Fig. 14. Experimental and numerical confrontation in terms of intrinsic dissipation fields during the chip segment formation (at 80% of evolution): (a) numerical results (b) experimental results.

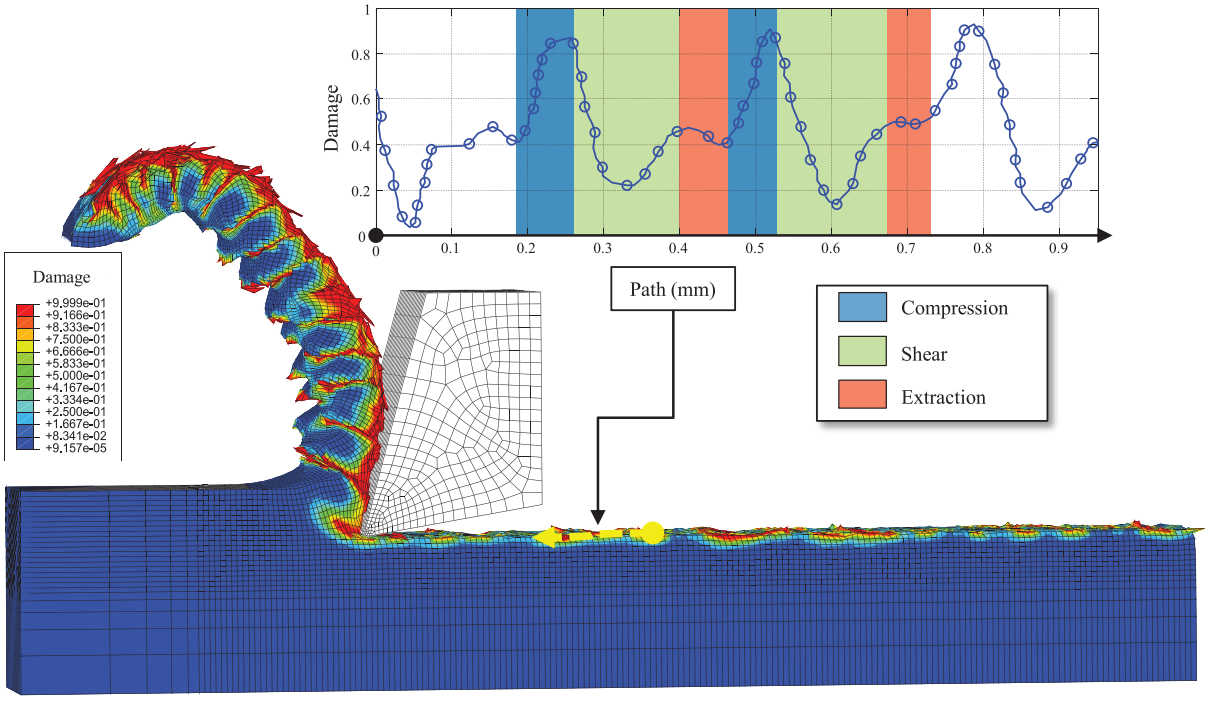

Fig. 15. Damage evolution profile along the generated surface and investigation of the impact of the different chip formation phases on the surface integrity. Case of test 2 ($Vc = 15$ m min^{-1}, $\gamma = 15°$, $f = 0.25$ mm).

ing of the final surface generation and its integrity. Accordingly, the exploitation of the presented model allows the prediction of the chip segmentation effect on the machined surface.

Fig. 15 depicts the damage distribution in the final part. A rippled damage tendency is observed along the predefined path which reflects the repetitive aspect of this phenomenon. Surprisingly, this tendency can be correlated with the chip formation steps (i.e compression, shear and extraction). It turns out that the three steps of the chip genesis are the source of this kind of damage tendency. Firstly, it's clearly perceptible that the compression phase induces always the most important damage magnitude. In fact, during this phase the segment stores the elastic energy which will be dissipated in the other stages. As results, many phenomena are observed, mainly: (i) the out of plane deformation phenomenon which impacts the final part in the form of a burr, (ii) the highest intrinsic dissipation and force levels, (iii) the development of the shear plane and the activation of the crack propagation phenomenon. These phenomena can explain the high level of the damage on the final part during this phase. Once the shear plane is created, the segment slides on it and the damage drops significantly. At the final step, the segment breaks free from the contact zone and continues to slide on both the cutting face and on the next segment. Hence, a progressive increase of the damage is observed which corresponds to the chip segment extraction but also (and probably more significantly) the initiation of the next one.

It is worth noticing that the analyzed machining videos show that the second and the third steps (i.e shear and extraction) are strongly conditioned by the first step. Consequently, one can therefore assume that the control of the compression chip formation phase can improve the surface integrity.

7. Conclusion and outlooks

The present work deals with the Ti-6Al-4V chip formation problem. It proposes, on one hand, a coupled in-situ measurement of thermal and

kinematic fields at micro-scale and on the other hand, a numerical investigation in order to restitute the experimental phenomena. This contribution provides a valuable insight on the thermomechanical couplings and thus gives a new understanding of the Ti-6Al-4V chip formation mechanisms.

In the first section, the strain, strain-rates, temperatures along with intrinsic dissipation fields are presented and discussed. The experimental observations highlighted the dependency of the physical phenomena to the machining parameters (i.e. cutting speed and the rake angle). Accordingly, it brings to light the cutting speed effect on the strain localization and also the geometric aspect of the shear angle by means of the rake angle variation. In addition, the crack propagation analysis conducted in this work emphasized the effect of the rake angle on the chip segment shape.

For confrontation sake, a 3D orthogonal cutting model is set up and computed for the same cutting conditions as in the presented experiments. In summary, it can be said that simulation results show a good agreement with experiments. It permits to predict the chip formation morphology, thermal and kinematics fields under an acceptable error. In addition, it provides a precious insight regarding the chip formation genesis and its influence on the surface integrity. Its 3D aspect which liberates the classical plane strain hypothesis and its simple modeling of behavior and material failure are among the strengths points of this FE model. However, several points should be improved for a better chip formation prediction and other configurations (cutting velocity, rake angle, feed...) can of course be investigated by the same mean and would be required to fully validate the proposed approach.

Two main drawbacks can be singled out of the presented FE orthogonal cutting model. The first one is the lack of knowledge on the tribological behavior of the tungsten carbide and the titanium alloy Ti-6Al-4V. Indeed, the determination of friction and the heat partition evolutions is an experimental challenge and constitutes a perspective of this work. For this purpose, the use of open tribometer that enables to reproduce as faithfully as possible the cutting condition (i.e. contact pressure, sliding velocity, ...) seems inevitable.

The second drawback of the proposed FE model is the material separation technique. It is a direct consequence of the chosen numerical procedure and induces a lack of information in the primary shear zone as discussed above. Other than element deletion, the node splitting and the adaptative remeshing techniques present as powerful alternative to overcome the problem [68–70]. Indeed, a correction of this numerical artefact should be addressed in future works.

Declaration of Competing Interests

The authors declare that they have no known competing financial interests or personal relationships that could have appeared to influence the work reported in this paper.

References

[1] Komanduri R, Turkovich BV. New observations on the mechanism of chip formation when machining titanium alloys. Wear 1981;69(2):179–88. doi:10.1016/0043-1648(81)90242-8.

[2] Barry J, Byrne G, Lennon D. Observations on chip formation and acoustic emission in machining Ti6Al4V alloy. Int J Mach Tools Manuf 2001;41(7):1055–70. doi:10.1016/S0890-6955(00)00096-1.

[3] Ducobu F, Rivière-Lorphèvre E, Filippi E. Numerical contribution to the comprehension of saw-toothed Ti6Al4V chip formation in orthogonal cutting. Int J Mech Sci 2014;81:77–87. doi:10.1016/j.ijmecsci.2014.02.017.

[4] Dandekar CR, Shin YC, Barnes J. Machinability improvement of titanium alloy (Ti-6Al-4V) via lam and hybrid machining. Int J Mach Tools Manuf 2010;50(2):174–82. doi:10.1016/j.ijmachtools.2009.10.013.

[5] Bermingham M, Palanisamy S, Dargusch M. Understanding the tool wear mechanism during thermally assisted machining Ti-6Al-4V. Int J Mach Tools Manuf 2012;62:76–87. doi:10.1016/j.ijmachtools.2012.07.001.

[6] Ayed Y, Germain G, Salem WB, Hamdi H. Experimental and numerical study of laser-assisted machining of Ti6Al4V titanium alloy. Finite Elem Anal Des 2014;92:72–9. doi:10.1016/j.finel.2014.08.006.

[7] Hong SY, Markus I, cheol Jeong W. New cooling approach and tool life improvement in cryogenic machining of titanium alloy Ti-6Al-4V. Int J Mach Tools Manuf 2001;41(15):2245–60. doi:10.1016/S0890-6955(01)00041-4.

[8] Sun S, Brandt M, Dargusch M. Machining Ti-6Al-4V alloy with cryogenic compressed air cooling. Int J Mach Tools Manuf 2010;50(11):933–42. doi:10.1016/j.ijmachtools.2010.08.003.

[9] Ezugwu E, Silva RD, Bonney J, Machado Á. Evaluation of the performance of CBN tools when turning Ti-6Al-4V alloy with high pressure coolant supplies. Int J Mach Tools Manuf 2005;45(9):1009–14. doi:10.1016/j.ijmachtools.2004.11.027.

[10] Arrazola P-J, Garay A, Iriarte L-M, Armendia M, Marya S, Maître FL. Machinability of titanium alloys (Ti6Al4V and Ti555.3). J Mater Process Technol 2009;209(5):2223–30. doi:10.1016/j.jmatprotec.2008.06.020.

[11] Bermingham M, Palanisamy S, Kent D, Dargusch M. A comparison of cryogenic and high pressure emulsion cooling technologies on tool life and chip morphology in Ti-6Al-4V cutting. J Mater Process Technol 2012;212(4):752–65. doi:10.1016/j.jmatprotec.2011.10.027.

[12] Sima M, Özel T. Modified material constitutive models for serrated chip formation simulations and experimental validation in machining of titanium alloy Ti-6Al-4V. Int J Mach Tools Manuf 2010;50(11):943–60. doi:10.1016/j.ijmachtools.2010.08.004.

[13] Sutter G, List G. Very high speed cutting of Ti-6Al-4V titanium alloy-change in morphology and mechanism of chip formation. Int J Mach Tools Manuf 2013;66:37–43. doi:10.1016/j.ijmachtools.2012.11.004.

[14] Harzallah M. Caractérisation in-situ et modélisation des mécanismes et couplages thermomécaniques en usinage : application á l'alliage de titane Ti-6Al-4V. Thése de doctorat dirigée par Landon, Yann et Pottier, Thomas Génie mécanique, mécanique des matériaux Ecole nationale des Mines d'Albi-Carmaux 2018; 2018. Ph.D. thesis.

[15] Calamaz M, Coupard D, Girot F. A new material model for 2D numerical simulation of serrated chip formation when machining titanium alloy Ti 6Al 4V. Int J Mach Tools Manuf 2008;48(3):275–88. doi:10.1016/j.ijmachtools.2007.10.014.

[16] Komanduri R. Some clarifications on the mechanics of chip formation when machining titanium alloys. Wear 1982;76(1):15–34. doi:10.1016/0043-1648(82)90113-2.

[17] Molinari A, Musquar C, Sutter G. Adiabatic shear banding in high speed machining of Ti-6Al-4V: experiments and modeling. Int J Plast 2002;18(4):443–59. doi:10.1016/S0749-6419(01)00003-1.

[18] Hua J, Shivpuri R. Prediction of chip morphology and segmentation during the machining of titanium alloys. J Mater Process Technol 2004;150(1):124–33. doi:10.1016/j.jmatprotec.2004.01.028.

[19] Pottier T, Germain G, Calamaz M, Morel A, Coupard D. Sub-millimeter measurement of finite strains at cutting tool tip vicinity. Exp Mech 2014;54(6):1031–42. doi:10.1007/s11340-014-9868-0.

[20] Harzallah M, Pottier T, Senatore J, Mousseigne M, Germain G, Landon Y. Numerical and experimental investigations of Ti-6Al-4V chip generation and thermomechanical couplings in orthogonal cutting. Int J Mech Sci 2017;134:189–202. doi:10.1016/j.ijmecsci.2017.10.017.

[21] Owen D, Vaz M. Computational techniques applied to high-speed machining under adiabatic strain localization conditions. Comput Methods Appl Mech Eng 1999;171(3):445–61. doi:10.1016/S0045-7825(98)00220-5.

[22] Johnson GR, Cook WH. Fracture characteristics of three metals subjected to various strains, strain rates, temperatures and pressures. Eng Fract Mech 1985;21(1):31–48. doi:10.1016/0013-7944(85)90052-9.

[23] Mabrouki T, Girardin F, Asad M, Rigal J-F. Numerical and experimental study of dry cutting for an aeronautic aluminium alloy (a2024-t351). Int J Mach Tools Manuf 2008;48(11):1187–97. doi:10.1016/j.ijmachtools.2008.03.013.

[24] Atlati S, Haddag B, Nouari M, Zenasni M. Analysis of a new segmentation intensity ratio sir to characterize the chip segmentation process in machining ductile metals. Int J Mach Tools Manuf 2011;51(9):687–700. doi:10.1016/j.ijmachtools.2011.05.007.

[25] Dorogoy A, Rittel D. Determination of the johnson–cook material parameters using the SCS specimen. Exp Mech 2008;49(6):881. doi:10.1007/s11340-008-9201-x.

[26] Germain G, Morel A, Braham-Bouchnak T. Identification of material constitutive laws representative of machining conditions for two titanium alloys: Ti6Al4V and Ti555-3. J Eng Mater Technol 2013;135(3):31002–11. doi:10.1115/1.4023674.

[27] Yaich M, Ayed Y, Bouaziz Z, Germain G. Numerical analysis of constitutive coefficients effects on fe simulation of the 2D orthogonal cutting process: application to the Ti6Al4V. Int J Adv Manuf Technol 2017;93(1):283–303. doi:10.1007/s00170-016-8934-4.

[28] Ducobu F, Riviére-Lorphévre E, Filippi E. On the importance of the choice of the parameters of the johnson-cook constitutive model and their influence on the results of a Ti6Al4V orthogonal cutting model. Int J Mech Sci 2017;122:143–55. doi:10.1016/j.ijmecsci.2017.01.004.

[29] Umbrello D, M'Saoubi R, Outeiro J. The influence of Johnson-Cook material constants on finite element simulation of machining of AISI 316L steel. Int J Mach Tools Manuf 2007;47(3):462–70. doi:10.1016/j.ijmachtools.2006.06.006.

[30] Zhang Y, Mabrouki T, Nelias D, Courbon C, Rech J, Gong Y. Cutting simulation capabilities based on crystal plasticity theory and discrete cohesive elements. J Mater Process Technol 2012;212(4):936–53. doi:10.1016/j.jmatprotec.2011.12.001.

[31] Owen D, Vaz M. Computational techniques applied to high-speed machining under adiabatic strain localization conditions. Comput Methods Appl Mech Eng 1999;171(3–4):445–61. doi:10.1016/S0045-7825(98)00220-5.

[32] Liu J, Bai Y, Xu C. Evaluation of ductile fracture models in finite element simulation of metal cutting processes. J Manuf Sci Eng 2013;136(February 2014):11010. doi:10.1115/1.4025625.

[33] Bao Y, Wierzbicki T. On the cut-off value of negative triaxiality for fracture. Eng Fract Mech 2005;72(7):1049–69. doi:10.1016/j.engfracmech.2004.07.011.

[34] Zhang YC, Mabrouki T, Nelias D, Gong YD. Chip formation in orthogonal cutting considering interface limiting shear stress and damage evolution based on fracture energy approach. Finite Elem Anal Des 2011;47(7):850–63. doi:10.1016/j.finel.2011.02.016.

[35] Bäker M. Finite element simulation of high-speed cutting forces. J Mater Process Technol 2006;176(1):117–26. doi:10.1016/j.jmatprotec.2006.02.019.

[36] Mabrouki T, Rigal J-F. A contribution to a qualitative understanding of thermo-mechanical effects during chip formation in hard turning. J Mater Process Technol 2006;176(1):214–21. doi:10.1016/j.jmatprotec.2006.03.159.

[37] Guo YB, Wen Q, Woodbury KA. Dynamic material behavior modeling using internal state variable plasticity and its application in hard machining simulations. J Manuf Sci Eng 2005;128(3):749–59.

[38] Abdelali HB, Claudin C, Rech J, Salem WB, Kapsa P, Dogui A. Experimental characterization of friction coefficient at the tool chip workpiece interface during dry cutting of aisi 1045. Wear 2012;286-287:108–15. doi:10.1016/j.wear.2011.05.030. Tribology in Manufacturing Processes

[39] Bonnet C, Valiorgue F, Rech J, Hamdi H. Improvement of the numerical modeling in orthogonal dry cutting of an AISI 316L stainless steel by the introduction of a new friction model. CIRP Journal of Manufacturing Science and Technology 2008;1(2):114–18. doi:10.1016/j.cirpj.2008.09.006. High Performance Cutting

[40] Hijazi a, Madhavan V. A novel ultra-high speed camera for digital image processing applications. Meas Sci Technol 2008;19(8):85503. doi:10.1088/0957-0233/19/8/085503.

[41] Baizeau T, Campocasso S, Fromentin G, Besnard R. Kinematic field measurements during orthogonal cutting tests via DIC with double-frame camera and pulsed laser lighting. Exp Mech 2017:581–91. doi:10.1007/s11340-016-0248-9.

[42] Zhang D, Zhang X-M, Xu W-J, Ding H. Stress field analysis in orthogonal cutting process using digital image correlation technique. J Manuf Sci Eng 2016;139(3). doi:10.1115/1.4033928.

[43] Zhang D, Zhang X-M, Ding H. Hybrid digital image correlation-finite element modeling approach for modeling of orthogonal cutting process. J Manuf Sci Eng 2018;140(4). doi:10.1115/1.4038998.

[44] Davis B, Dabrow D, Ifju P, Xiao G, Liang SY, Huang Y. Study of the shear strain and shear strain rate progression during titanium machining. J Manuf Sci Eng 2018;140(5). doi:10.1115/1.4038891.

[45] Baizeau T, Campocasso S, Rossi F, Poulachon G, Hild F. Cutting force sensor based on digital image correlation for segmented chip formation analysis. J Mater Process Technol 2016;238:466–73. doi:10.1016/j.jmatprotec.2016.07.016.

[46] Kazban RV, Vernaza Peña KM, Mason JJ. Measurements of forces and temperature fields in high-speed machining of 6061-t6 aluminum alloy. Exp Mech 2008;48(3):307–17. doi:10.1007/s11340-007-9069-1.

[47] Zhang D, Zhang X-M, Ding H. A study on the orthogonal cutting mechanism based on experimental determined displacement and temperature fields. Procedia CIRP 2016;46:35–8. doi:10.1016/j.procir.2016.03.176. 7th HPC 2016 - CIRP Conference on High Performance Cutting

[48] Arriola I, Whitenton E, Heigel J, Arrazola P. Relationship between machinability index and in-process parameters during orthogonal cutting of steels. CIRP Ann 2011;60(1):93–6. doi:10.1016/j.cirp.2011.03.082.

[49] Harzallah M, Pottier T, Gilblas R, Landon Y, Mousseigne M, Senatore J. A coupled in-situ measurement of temperature and kinematic fields in Ti-6Al-4V serrated chip formation at micro-scale. Int J Mach Tools Manuf 2018;130–131:20–35. doi:10.1016/j.ijmachtools.2018.03.003.

[50] Vacher P, Dumoulin S, Morestin F, Mguil-Touchal S. Bidimensional strain measurement using digital images. Proc Inst Mech Eng Part C 1999;213(8):811–17. doi:10.1243/0954406991522428.

[51] Pan B, Dafang W, Yong X. Incremental calculation for large deformation measurement using reliability-guided digital image correlation. Optics and Lasers in Engineering 2012;50(4):586–92. doi:10.1016/j.optlaseng.2011.05.005. Computational Optical Measurement

[52] Basak D, Overfelt RA, Wang D. Measurement of specific heat capacity and electrical resistivity of industrial alloys using pulse heating techniques. Int J Thermophys 2003;24(6):1721–33. doi:10.1023/B:IJOT.0000004101.88449.86.

[53] Boivineau M, Cagran C, Doytier D, Eyraud V, Nadal MH, Wilthan B, et al. Thermophysical properties of solid and liquid Ti-6Al-4V (TA6V) alloy. Int J Thermophys 2006;27(2):507–29. doi:10.1007/PL00021868.

[54] Barge M, Hamdi H, Rech J, Bergheau J-M. Numerical modelling of orthogonal cutting: influence of numerical parameters. Journal of Materials Processing Technology 2005;164-165:1148–53. doi:10.1016/j.jmatprotec.2005.02.118. AMPT/AMME05 Part 2

[55] Zorev N.N. Inter-relationship between shear processes occurring along tool face and on shear plane in metal cutting1963;42–49Cited By :15;

[56] Childs T, Mahdi M, Barrow G. On the stress distribution between the chip and tool during metal turning. CIRP Ann 1989;38(1):55–8. doi:10.1016/S0007-8506(07)62651-1.

[57] Grzesik W. Experimental investigation of the influence of adhesion on the frictional conditions in the cutting process. Tribol Int 1999;32(1):15–23. doi:10.1016/S0301-679X(99)00004-3.

[58] Courbon C, Pusavec F, Dumont F, Rech J, Kopac J. Tribological behaviour of Ti6Al4V and inconel718 under dry and cryogenic conditions application to the context of machining with carbide tools. Tribol Int 2013;66:72–82. doi:10.1016/j.triboint.2013.04.010.

[59] Bowden FP, Tabor D. The friction and lubrication of solids. New York: Oxford Univ. Press; 1950. p. 337. doi:10.1126/science.113.2938.443-a. Science 113(2938):443444, 1951.

[60] Rech J, Arrazola P, Claudin C, Courbon C, Pusavec F, Kopac J. Characterisation of friction and heat partition coefficients at the tool-work material interface in cutting. CIRP Ann 2013;62(1):79–82. doi:10.1016/j.cirp.2013.03.099.

[61] BLOK H. Theoretical study of temperature rise at surfaces of actual contact under oiliness lubricating conditions. Proc Inst Mech Eng 1937;2:222. doi:10.1016/0043-1648(63)90283-7.

[62] JAEGER JC. Moving sources of heat and the temperature of sliding contacts. J Proc Roy Soc New South Wales 1942;76:202.

[63] Bauzin JG, Laraqi N, Baïri A. Estimation of thermal contact parameters at the interface of two sliding bodies. J Phys 2008;135:12015. doi:10.1088/1742-6596/135/1/012015.

[64] Brocail J, Watremez M, Dubar L. Identification of a friction model for modelling of orthogonal cutting. Int J Mach Tools Manuf 2010;50(9):807–14. doi:10.1016/j.ijmachtools.2010.05.003.

[65] Longére P., Dragon A.. Thermodynamics based evaluation of the plastic work induced heating. consequences on the dynamic localization conditions2009;:1257–1262.

[66] Dorothy HL, Longére P. Modelling of high strain rate adiabatic shear banding induced failure: a comparison of two approaches. Int J Impact Eng 2017;110:219–27. doi:10.1016/j.ijimpeng.2017.02.024. Special Issue in honor of Seventy Fifth Birthday of Professor N. K. Gupta

[67] Macdougall D, Harding J. A constitutive relation and failure criterion for Ti6Al4V alloy at impact rates of strain. J Mech Phys Solids 1999;47(5):1157–85. doi:10.1016/S0022-5096(98)00086-6.

[68] Strenkowski JS, Carroll JT III. A finite element model of orthogonal metal cutting. J Eng Ind 1985;107(4):349–54.

[69] Calamaz M, Coupard D, Girot F. Numerical simulation of titanium alloy dry machining with a strain softening constitutive law. Mach Sci Technol 2010;14(2):244–57.

[70] Zeramdini B, Robert C, Germain G, Pottier T. Numerical simulation of metal forming processes with 3D adaptive remeshing strategy based on a posteriori error estimation. Int J Mater Form 2018. doi:10.1007/s12289-018-1425-4.